



UNIVERSITATEA BABEȘ-BOLYAI
BABEȘ-BOLYAI TUDOMÁNYEGYETEM
BABEȘ-BOLYAI UNIVERSITÄT
TRADITIO ET EXCELLENTIA

Laser Induced Photoelectron Holography in Diatomic Molecules

Ph.D. thesis
SUMMARY

GELLÉRT ZSOLT KISS

SCIENTIFIC SUPERVISOR
PROFESSOR DR. LADISLAU NAGY

FACULTY OF PHYSICS, BABEȘ-BOLYAI UNIVERSITY
CLUJ-NAPOCA, ROMANIA
2019

GELLÉRT ZSOLT KISS

**Laser Induced Photoelectron Holography in
Diatomic Molecules**

SUMMARY

Ph.D. Thesis

presented to the Faculty of Physics,
Babeş-Bolyai University, Cluj-Napoca, Romania

2019

Abstract

Laser physics and technology has become a highly developing field of science in the recent years. With the remarkable achievements in the production of ultrashort and intense laser pulses new horizons have been opened for scientists to investigate ultrafast phenomena taking place at atomic level and to manipulate matter below the microscopic size. In parallel to the impressive developments in the laboratories the newly emerging and not completely understood processes needed to be explained by elaborate theoretical works.

The present thesis aims to deliver novel and useful knowledge to the broad theoretical field of laser-matter interaction, by investigating - with the use of first principle calculations - laser induced ultrafast processes taking place in small atomic systems in the presence of ultrashort XUV radiation fields.

In the first part of this work the theory behind the laser-atom/molecule interaction is detailed in the framework of the *single active electron approximation*, then different theoretical methods are presented by comparing the results obtained by their numerical implementation for the hydrogen atom.

In the main part of the present thesis, first the development and the implementation of a numerical method based on the direct solution of *time-dependent Schrödinger equation* for diatomic molecules is presented, and then this is employed to investigate the laser induced electron dynamics and the *photoelectron holography* in the H_2^+ molecule.

Finally, the conclusions are drawn, mainly on how the intensity of the laser field and the internuclear distance - via the value and the spatial profile of the binding potential - influence the *photoelectron spectra* and the interference patterns, that appear in the photoelectron hologram of the molecular target.

Keywords

Ultrashort and intense laser fields

Diatomic molecules

Time-Dependent Schrödinger Equation (TDSE)

Single Active Electron approximation (SAE)

Laser induced electron wave packet (EWP) dynamics

Photoelectron Holography (PEH)

Contents of the Thesis

1	Introduction to laser technology	6
2	Laser-matter interaction	11
2.1	Principle of lasers	11
2.2	Maxwell's equations for describing the laser field	16
2.3	Charged particle in laser field	19
3	Laser induced processes in atoms and molecules	24
3.1	Photoexcitation and ionization mechanisms	24
3.2	High Harmonic Generation (HHG)	30
4	Photoelectron holography	33
5	Theoretical methods for investigating laser induced electron dynamics	38
5.1	Semi-classical approaches: Strong Field Approximation methods	38
5.1.1	Theory and Results: SFA+ approach for HHG calculations	40
5.2	Methods for the solution of the time-dependent Schrödinger equation (TDSE)	44
5.2.1	Representation of the wave function	44
5.2.2	Temporal propagation algorithms for the wave function	50
5.2.3	Direct solution of the TDSE (in momentum space)	53
5.2.4	Iterative solution of the TDSE (in momentum space)	54
5.2.5	Comparison of the implemented TDSE methods	57
6	TDSE for diatomic molecules	61
6.1	The Hamiltonian	61
6.1.1	The field-free Hamiltonian	61
6.1.2	Interaction with the laser field	62
6.2	Coordinate systems for laser-molecule interaction	63
6.3	TDSE in the prolate spheroidal coordinates	64
6.4	TDSE on Finite Element Discrete Variable Representation grids	66
6.4.1	Using the matrix formalism	68
6.4.2	Symmetrization of the Hamiltonian matrix	70

6.5	Temporal propagation of the wave function	73
6.6	Calculation of physical quantities	76
6.6.1	The norm of the wave function	76
6.6.2	Occupation probabilities of electronic bound states	77
6.6.3	The expected position of the ejected electron	78
6.6.4	Calculating the photoelectron spectrum	79
6.7	A possible extension of the method: the inclusion of the nuclear motion	82
7	The H_2^+ molecule in ultrashort XUV laser fields	84
7.1	Numerical details	84
7.2	Electronic bound states and energies of H_2^+	85
7.2.1	Identification of bound state symmetry	86
7.2.2	The convergence of bound state energies and wave functions	87
7.3	XUV laser induced electron dynamics - Photoexcitation of H_2^+	93
7.4	Holographic Mapping of the H_2^+ target	99
7.4.1	Calculating convergent photoelectron holograms	101
7.4.2	The effect of the molecular potential on the photoelectron hologram	110
7.4.3	Photoelectron spectra as a function of laser field intensity	117
8	Conclusions and outlook	120
	Acknowledgements	124
	List of Publications	126
	Appendix I: Atomic Units	129
	Appendix II: Coordinate Transformations	130
	Bibliography	138

Contents of the Summary

1	Introduction	7
1.1	Photoelectron Holography	9
2	Theory	13
2.1	Theoretical methods for investigating laser induced electron dynamics	13
2.2	TDSE for diatomic molecules	17
3	Results and discussion	23
3.1	Convergent bound state wave functions and bound state energies of H_2^+	23
3.2	XUV-field induced electron dynamics: Photoexcitation of H_2^+	24
3.3	The ionization of H_2^+ : Obtaining convergent photoelectron spectra	26
3.4	The effect of the laser field intensity on the photoelectron hologram	30
3.5	The effect of the molecular potential on the photoelectron hologram	32
4	Conclusions	37
	List of Publications	40
	List of Abbreviations	42
	Bibliography (selected References)	45

1. Introduction

In the last decades laser science has become the most promising tool for detailed investigations of ultrafast phenomena taking place at atomic scales, and for matter manipulation with high energy concentrations. The "light amplification by stimulated emission [1] of radiation" (laser) [2] technique, which produces highly coherent and monochromatic light beams, was implemented first in experiments in 1960 [3], since then lasers have become routinely used in a wide array of applications in our daily life. These applications include industrial utilizations (e.g., material processing), commercial uses in optical communications and computer technology (e.g., data transfer via optical fibers, data storage on optical discs), military (e.g., missile guidance) or medical applications (laser-assisted surgeries [4–8]).

With the continuous progress in laser technology higher and higher power beams of coherent light have been produced, while shorter and shorter laser pulse durations achieved. This has opened new perspectives in the investigations in the domains of fundamental sciences [9], where for instance the laser-driven fusion [10] or laser-assisted drug synthesis [11] are desired to be achieved with high efficiencies. The possibility of producing high power lasers began with the year 1985, when the "chirped pulse amplification" (CPA) method was invented by Donna Strickland and Gérard Mourou¹, and which technique is used since in worldwide laser-facilities for amplifying ultrashort ($< 10 \text{ fs} = 10^{-14} \text{ s}$) pulses above 10^{15} W/cm^2 intensity. Moreover, by the implementation of the momentous laser facility, Extreme Light Infrastructure, which is based until now on three different pillars: ELI-Beamlines Prague (Czech Republic), ELI Attosecond Light Pulse Source (ELI-ALPS) Szeged (Hungary), and ELI Nuclear Physics (ELI-NP) Măgurele (Romania) [12], new horizons have become accessible for the international laser community, where the aspiration to operate within extreme conditions has become a daily routine.

Due to the emergent technique of focusing high intensity pulses onto atomic systems and operating with ultrashort time scales, new and previously not entirely understood phenomena can be induced and investigated at the nanoscopic scale and below that. The most well known phenomenon that occurs during the interaction between an incident electromagnetic (EM) wave and matter is the *photoelectric effect*, when the target system is ionized by the emission of a bound electron. This effect and the previous observations, according to which regardless of the EM field intensity, light may eject electrons even at low intensities was first explained by Albert Einstein in 1905 [15], when he proposed that a light beam can be considered as a collection of discrete wave packets, i.e. photons, each having a given ν frequency and energy $\varepsilon_\nu = h\nu$ ($h \simeq 6.626 \times 10^{-34} \text{ Js}$ is the Planck constant [16]). According to the simplest picture during the photoemission process a bound electron (having the

¹Donna Strickland and Gérard Mourou were awarded the Nobel Prize in Physics on 2nd of October 2018 for their joint work on CPA

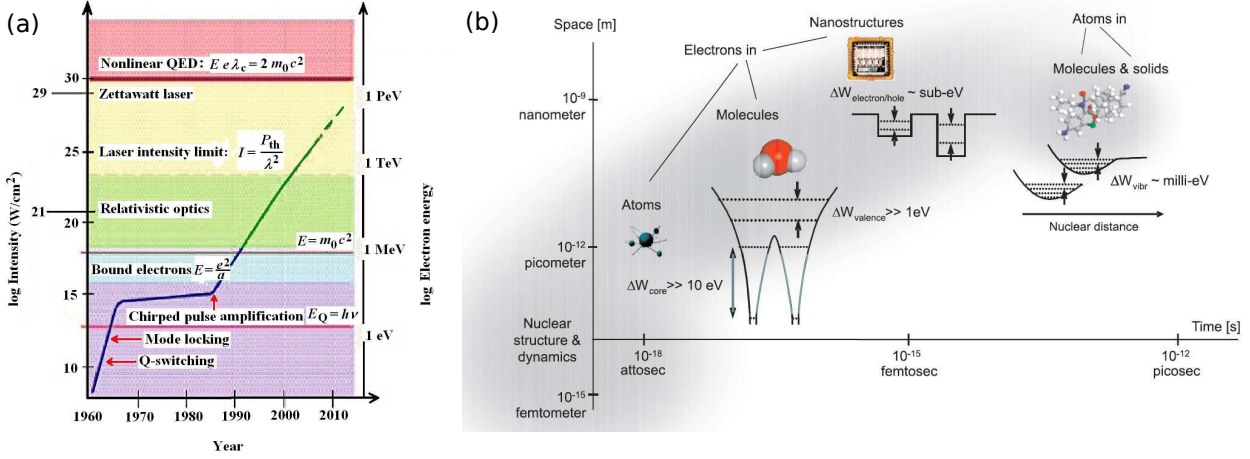


Figure 1.1: (a) Progress in achievable light intensity with the year. The solid curve shows a continuous increase having two large slopes, first around the year 1960 (the invention of the laser), and another one starting from 1985 (the invention of the CPA technique). The figure is adapted from Mourou and Yanovsky (2004) c 2004 OSA [13]. (b) Time scales and characteristic lengths for dynamics in atoms and molecules. Adapted from [14].

bound energy $\varepsilon_b < 0$) absorbs a single photon from the radiation field and after this it is released with the kinetic energy $\varepsilon_k = h\nu - I_p$, where $I_p = |\varepsilon_b|$ represents the ionization potential, and k is the electron's final momentum. In the particular case when the energy of the absorbed photon is lower than I_p , but equal to the energy difference between two bound states $h\nu = \varepsilon_{b'} - \varepsilon_b$, a process called *photoexcitation* takes place, during which the electron is carried by the pumped energy from a lower energy level b to the higher level b' .

Moreover, it was later observed, that when the radiation field is a high intensity ($> 10^{10}$ W/cm²) laser field, depending on the field's parameters next to the single photon ionization other ionization processes may appear as well, such as the multi-photon (MPI) or above-threshold ionization (ATI), tunneling ionization (TI), or over-the-barrier ionization (OBI) (see Figure 1.2). In order to identify the dominant ionization mechanism, Keldysh introduced a laser and target dependent parameter (*Keldysh parameter*) $\gamma = \sqrt{I_p/2U_p} \sim E_0^{-1} \lambda^{-1} I_p^{1/2}$, where $U_p = e^2 E_0^2 / \sqrt{4m_e \omega^2}$ is the ponderomotive energy, i.e., cycle-averaged energy gained by the emitted electron driven in the radiation field. When the $\gamma \gg 1$ condition is fulfilled it means that the quiver energy of the continuum electron is much less than I_p of the target, and the binding potential is not significantly distorted by the radiation field. In this case the photoemission occurs predominantly via single or multiphoton absorptions. In the other limit, when $\gamma \ll 1$ either the external field's amplitude E_0 is very high, or the wavelength λ is large (\sim IR waves), meaning that the period of the laser field $T = \lambda/c$ is also sufficiently large to favorize the quasi-static tunneling photoemission through the distorted binding potential [17]. The transition between the two regimes, i.e., around $\gamma \approx 1$, is a smooth one, since it was observed that by approaching γ to 1 starting from the multiphoton regime the ATI peaks start to fade out gradually until they almost completely vanish.

In other scenarios - succeeding the primary photoionization of the target - the ejected

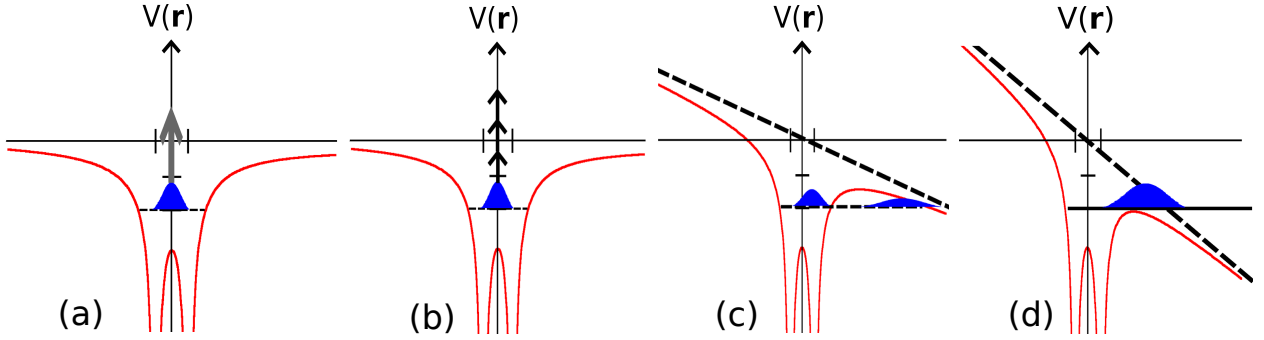


Figure 1.2: The schematics of different ionization mechanisms: (a) single-photon ionization; (b) multi- and above-threshold ionization; (c) tunneling ionization; (d) over-the-barrier ionization. The red curves show the 1D profile of the H_2^+ diatomic molecule's Coulomb potential $V(\vec{r})$, which for higher laser intensities [the case of (c) and (d)] gets distorted by the electron-laser interaction term $U_{\text{int}}(t) = \vec{r} \cdot \vec{E}(t)$ in atomic units (dashed black lines), where \vec{r} is the electron's position vector, while $\vec{E}(t)$ the electric component of the laser field.

electron may be driven back by the radiation field in the close vicinity of the parent ion, where it may be reabsorbed by this [*High Harmonic Generation* (HHG) process], or on which the returned electronic wave packet (EWP) may re-scatter elastically or inelastically. The first post-ionization scenario enjoys a strong interest in the field of attoscience, namely in the production of high energy XUV ultrashort pulses, since in the HHG mechanism the energy gained by the ejected electron from the laser field is emitted in a form of a high frequency photon [18], and by using an appropriate phase-matching the created photons are coherently added and XUV attosecond pulses can be produced.

1.1 Photoelectron Holography

In the later scenarios the re-scattering EWP may be diffracted by the residual ion, and a diffraction pattern occurs [*laser-induced electron diffraction* (LIED)] [19] in the measured photoelectron spectra (PES), which then can be used to extract structural information - via laborious procedures - regarding the irradiated target. Alongside this, recent studies [20,21] have suggested that well distinguishable radial fringe structures (which implicitly simplify the procedure of structural information extraction) may appear in the PES as the consequence of an alternative process, according to which two distinct EWPs that are following different paths interfere: the first one is the re-scattered wave on the ion, while the second one is an electronic - unscattered or weakly scattered - wave, which is associated with a larger transverse momentum and consequently misses the residual ion (Figure 1.3). Similarly to the traditional holography, where two distinct fully coherent electromagnetic waves are present - i.e., a scattered and a direct wave - in this laser induced EWP dynamics scenario a scattered electronic wave interferes with a fully coherent direct wave, hence the process itself can be considered as the laser induced *photoelectron holography* PEH of the target. The presence of these different EWP paths will lead to different phases accumulated by these, and the resulted phase differences become detectable in the measured photoelectron spectra (i.e.,

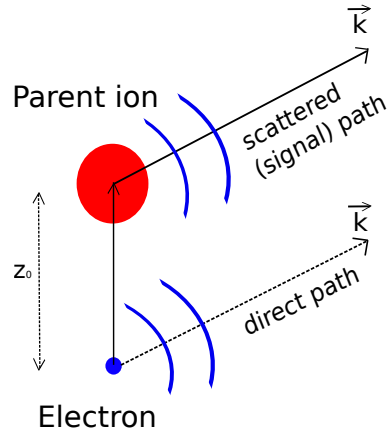


Figure 1.3: The schematics of the scattered and direct electron trajectories. The parameter z_0 indicates the maximum distance the signal (strongly scattered) electron reached before the rescattering event.

in the *angle-resolved momentum distribution* of the ejected electrons), that may deliver us useful structural information about the irradiated atomic systems.

Previous investigations [21] demonstrated that the *spatial interference* of the EWPs detectable in the photoelectron spectra is the result of the superposition of wave packets 'born' approximately at the same time (i.e., during the same quarter-cycle of the laser pulse), but driven by the oscillating field along different paths. Due to the different phases accumulated by the two EWPs, the coherent superposition of these will lead to the formation of radial ridge structures in the PES [20, 22–28]. Using classical trajectory Monte-Carlo simulations [26] the assumption according to which these two distinct trajectories [20, 21] are present in the coherent superposition process was proven to be valid for the case of the hydrogen atom, where it was shown that the electrons can arrive at a given continuum state with a well defined momentum \vec{k} along a weakly scattered and a strongly scattered trajectory. Moreover, it was found that the weakly scattered electron, after it had been driven back by the oscillating field, approached the parent ion to the minimum distance of 5 atomic units; while the strongly scattered electron approached the core more closely, by reaching a ~ 1 a.u. separation distance from this [26].

By reviewing the literature of previous experimental [20, 22] and theoretical [26–30] investigations several aspects of the creation of the photoelectron holograms can be understood. Firstly, it was shown that for a given target the density of the interference minima is determined by the z_0 maximum distance measured from the parent ion that the liberated electron reached before the rescattering event. The value of z_0 can be directly controlled by the parameters of the driving field; i.e., by increasing the wavelength or the intensity of the laser pulse results in an increased z_0 value. Secondly, it was recently demonstrated [27] for atomic targets that for a fixed driving field the features of the hologram were strongly influenced by the profile of the scattering potential (i.e., by the atomic species). In addition to that, it was proven by first principle and classical trajectory calculations [27], that the phase accumu-

lated by the scattered electron is strongly influenced by the depth of the binding potential experienced by the rescattering electron along the returning path.

With real optimism, in the near future it might be possible for experimentalists to take advantage of this high target sensitivity of the PEH and utilize the measured photoelectron momentum distribution maps to identify local potentials inside the laser irradiated samples.

Previous studies on PEH of small molecules (H_2^+)

Besides atomic targets, several studies on the photoelectron holography of molecular targets were also performed [31–36], a large portion of which were focusing on smaller atomic systems, such as the H_2^+ molecule. The physics behind the creation of the photoelectron holograms in molecules and the features appearing in the PES can be more easily understood by investigating less complex targets. The H_2^+ molecule gives us the possibility to study the influence of the internuclear distance and the two-center interference of the EWPs on the molecular photoelectron holograms. A significant portion of H_2^+ related works [32, 33, 36] investigated the influence of the molecular axis orientation on the PEH at equilibrium internuclear distance, and found that the forward scattering hologram (the signal and reference EWPs were born at the same optical quarter cycles) is only weakly influenced by it. This weak effect was explained by the observation that in the case of small molecules the electron scattering cross section in the forward scattering direction is mainly determined by the long-range Coulomb potential [34, 37] and the short-range effects are repressed by the long range contribution. However, it was later shown that the molecular axis orientation dependence of the forward scattering photoelectron hologram can be increased either by using circularly polarized driving fields [38], or by increasing the molecular axis length [39]. For the backward scattering direction the contribution of the short-range part of the molecular Coulomb potential is larger, thus - as it was expected - the backward scattering PEH (where the signal and reference wave packets were created during different quarter cycles [31, 34]) is severely affected by the molecular axis orientation [34].

In contrast, investigations on the molecular axis length dependence of the forward scattering photoelectron holography are rather sparse. In [34] the indirect experimental evidence is presented on the molecular axis length dependence of the PEH. Furthermore, in the framework of a simplified model, where the H_2^+ was described by a 2D soft-core Coulomb potential, this effect was explicitly studied in [39] and [35]. However, in the first study [39] it was only marginally discussed, while in the second one [35] it was investigated in details only at large internuclear distances (in the region of the charge-resonance enhanced ionization).

Outline of the thesis

Due to the newly emergent and previously discussed phenomena, resulted from the interaction between matter and ultrashort, high intensity radiation fields, a correct understanding of the underlying processes is required. This can be achieved by extensive and elaborate theoretical investigations (e.g., [40–42]), which on the other hand will play an important role to generate further directions for experimentalists and for new technical developments in the field of laser science and technology. The present work is a theoretical one, which aims to deliver additional and deeper understanding - by the development of efficient numerical tools - in the field of laser induced electron dynamics, mainly to decipher the features appearing in the photoelectron spectra of the diatomic (H_2^+) molecule. The work, as it will be presented in the following sections, is based on first principle calculations.

In the above outlined context, the principal part of the present thesis is mainly dedicated to the investigation of the molecular axis length dependence of the forward scattering photoelectron hologram, where special attention is accorded to the physics of the molecular axis length dependence of the PEH. More precisely, this work concentrates mainly on the investigation of photoelectric holograms appearing as a result of the interaction between ultrashort XUV pulses and the H_2^+ target. The main goal was to acquire valuable knowledge regarding how the geometry (the internuclear distance) of the simplest molecule influences the nature of the HM pattern, and to identify the multi-center effects of the molecular binding potential on the holograms, as outlined in the second part of this thesis.

2. Theory

Theoretical works found in the literature, which investigate laser-induced electron dynamics may be separated into two separated parts. When certain specific aspects of the underlying mechanisms need to be studied, many works are restricted to semi-classical calculations that are using approximations and are focusing on the well defined problem (e.g., *strong field approximation* methods for calculating HHG spectra resulted by the reabsorbed laser-driven photoelectrons). These type of methods that in certain circumstances neglects some physical terms, usually treat (\sim partly) the electron semi-classically and are employed to obtain relevant information in a relative short computational time. However, in order to avoid as much as possible all information losses about the complete physical picture of the underlying processes (induced by laser fields in atomic systems), the most accurate methods used are based on the solution of the time-dependent Schrödinger Equation (TDSE); which on the other hand, even for the simplest case (the interaction between the hydrogen atom and a linearly polarized laser pulse) request a considerably larger amount of computer time than the first type of methods. In this later, 'exact', solutions of the TDSE, the electronic wave function is calculated in time, by propagating it with the use of the time-dependent Hamiltonian, that describes the entire system (atomic systems in laser fields).

2.1 Theoretical methods: implementations and benchmarking the codes (H atom in laser fields)

Semi-classical approaches: Strong Field Approximation methods

In those cases when for instance the spectra of the emitted HHG photons need to be calculated and investigated for different laser pulse parameters, different variation of the *strong field approximation* (**SFA**) method can be used to describe the motion of the laser-emitted, laser-driven and finally reabsorbed electrons. The dynamics of the returned and reabsorbed electron, that releases its kinetic energy gained from the oscillating field in the form of a high frequency photon (integer multiple of the fundamental driving frequency), can be described in the simplest way be employing the three-step model (TSM), according to which the reabsorbed electron, first, was ionized via the tunneling process (through the barrier of the laser-distorted Coulomb potential); then accelerated in the continuum by the oscillating electric field, where the Coulomb interaction with its parent ion is neglected; finally, after the laser field reverses its sign it is driven back by this, and it gets reabsorbed on its initial - ground - state. The motion of these electrons can be described by calculating

the time-dependent dipole moment [43]:

$$\vec{d}(t) = -i \int_{t_0}^t dt' \int d\vec{k} d_{\text{rec},\vec{r}}^*(\vec{k} + \vec{A}(t)) \exp \left[-iS_0(\vec{k}, t, t') \right] d_{\text{ion},\vec{r}}(\vec{k} + \vec{A}(t'), t') + c.c.,$$

where *c.c.* stands for the complex conjugate of the first part, $\vec{A}(t') = -\int_{-\infty}^{t'} \vec{E}(t'') dt''$ is the vector potential of the linearly polarized laser field within the dipole approximation, $d_{\text{ion},z} = \langle \Psi_{\vec{k}} | \hat{U}_{\text{laser}}(t') | \varphi_0 \rangle = \langle \Psi_{\vec{k}} | zE(t') | \varphi_0 \rangle$ is the probability amplitude for the $|\varphi_0\rangle \rightarrow |\Psi_{\vec{k}}\rangle$ transition ($|\varphi_0\rangle$ being the ground, while $|\Psi_{\vec{k}}\rangle$ the continuum state: usually Volkov states, or the more simpler plane waves), $S_0 = \int_{t'}^t dt'' [(\vec{k} + \vec{A}(t''))^2/2 + I_p]$ is the quasi-classical action (a phase factor the electron acquires during its excursion in the continuum from the radiation field), $d_{\text{rec},z}^* = \langle \varphi_0 | -z | \Psi_{\vec{k}} \rangle$ is the probability (transition) amplitude that the electron recombines with the residual ion by being reabsorbed on its initial ground state.

Extension of this method (**SFA+ approach**) would also consider the Stark-shift of the ground state during the recollision event, and calculating directly the time-dependent acceleration of the dipole moment $a(t) = \langle \Psi(t) | \hat{a} | \Psi(t) \rangle$ [with $\hat{a} = -(q/m_e)\partial V_c/\partial z$], the Fourier-transform of which is linearly proportional to the total power radiated by the non-relativistic electron [$P(\omega) = (e^2)/(6\pi\epsilon_0 c^3) \mathcal{F}\{a(t)\}$, with e being the elementary charge], i.e., the spectra of the emitted photons during the acceleration of an electrically charged particle. By using the Green-propagator formalism of the TDSE:

$$-i|\Psi(t)\rangle = G_0^+(t, t_0)|\Psi(t_0)\rangle + \int_{t_0}^t dt' G^+(t, t') U(t') G_0^+(t', t_0) |\Psi(t_0)\rangle,$$

where $U(t') = \vec{A}(t') \cdot \vec{k} + \vec{A}^2(t')/2$ (laser-electron interaction term in velocity gauge), and the Green functions: $G_0^+ = -i \exp\{-i(t - t_0)\mathcal{E}_0\}$, $G^+(t, t') = -i \exp\{-i \int_{t'}^t \mathcal{E}_{\vec{k}}(t'') dt''\}$. By employing the projection operators onto the bound and continuum states: $\hat{B} = \sum_{b=0}^{\infty} |\varphi_b\rangle \langle \varphi_b|$ and $\hat{C} = \int d\vec{k} |\vec{k}\rangle \langle \vec{k}|$, the dipole acceleration of the reabsorbed electron can be deduced to the relation

$$a(t) \simeq \langle \Psi(t) | \hat{B} \hat{a} \hat{C} | \Psi(t) \rangle + c.c. \equiv - \int d\vec{k} \frac{k^2/2 - \mathcal{E}_0}{\Delta_s} a_b(\vec{k}, t) + c.c..$$

In the equation above $a_b(\vec{k}; t)$ is calculated by solving the following differential equation by using fourth-order Runge-Kutta method [44, 45],

$$\frac{da_b(\vec{k}; t)}{dt} = i \left[\mathcal{E}_0 - \mathcal{E}(\vec{k}; t) \right] a_b(\vec{k}; t) + i C_F \langle \varphi_0 | \hat{a} | \vec{k} \rangle U(\vec{k}; t) \langle \vec{k} | V_c | \varphi_0 \rangle,$$

where for the case of the H atom: $V_c = -1/r$, the Coulomb factor $C_F = [2Z^2/n^2 E_0]$, $n = 1$, $Z = 1$, and $\mathcal{E}(\vec{k}, t) = k^2/2 + U(\vec{k}; t)$, while $\Delta_s = \delta t_s^{-1} \int_{t-\delta t_s}^t U(\vec{k}; t') dt'$ gives the Stark-shift of the ground during the δt_s recollision time, which is approximated as the ratio between the size of the wave packet $d_{\text{WP}} \simeq \tau_{\text{excursion}} \cdot v_{\text{initial}} \approx (3/4)2\pi/\omega_0 \cdot \sqrt{2|\varepsilon_0|}$ and the recollision

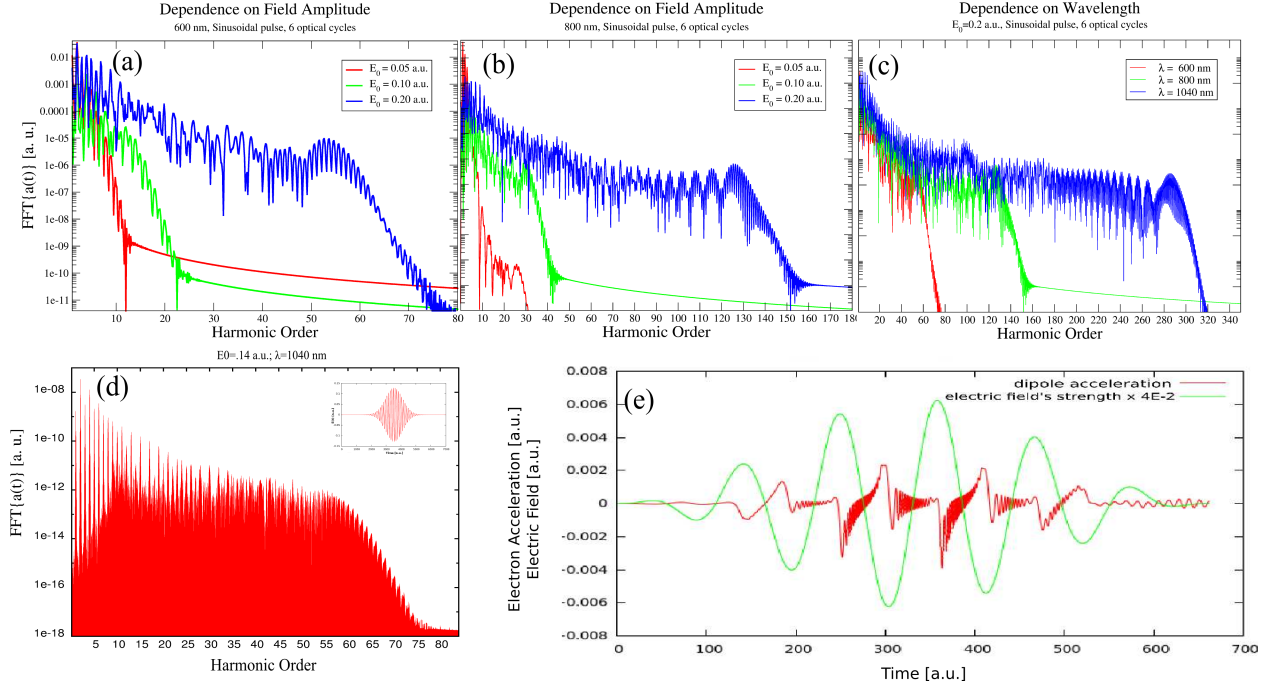


Figure 2.1: HHG spectra for the H atom using 6 cycle sinusoidal envelope pulses (a)-(c) and a 64 cycle Gaussian profile beam (d) for different laser field parameters. (a) $\lambda=600$ nm and (b) $\lambda=800$ nm show the extent of the plateau region depending on the E_0 electric field's amplitude. On subfig. (c) for a fixed intensity the HHG spectra dependence as a function of λ is shown. In subfigure (d) $E_0 = 0.14$ a.u.; $\lambda = 1040$ nm. (e) The $E(t)$ electric field component of the laser field (green curve), and the dipole acceleration $a(t)$ (red curve).

velocity of the highest energy electrons $v_{\text{recoil}} \approx \sqrt{2 \times 3.17U_p}$ (i.e., $\delta t_s = d_{\text{WP}}/v_{\text{recoil}}$).

TDSE methods: temporal propagation of the wave function

More complete picture regarding the laser-induced electron dynamics can be achieved by solving - numerically - the *electronic time-dependent Schrödinger equation* (TDSE). Usually the electronic wave function is expressed in terms of some basis functions (e.g., Bessel-functions, n-order polynomial functions, eigenfunctions of the field-free Hamiltonian etc.):

$$\Psi(\vec{r}; t) = \int d\vec{k} c(\vec{k}; t) \Psi_V(\vec{k}, \vec{r}; t),$$

where in the present case the use of the Volkov wave functions (solutions of the TDSE for electrically charged particle in radiation field) were considered together with the $c(\vec{k}; t)$ expansion coefficients, where \vec{k} is the momentum of the ejected electron; and then inserted the above expression into the TDSE:

$$i \frac{\partial}{\partial t} \Psi(\vec{r}; t) = \left[\hat{\mathcal{P}}^2/2 + \hat{U}_{\text{int}}(t) + V(\vec{r}) \right] \Psi(\vec{r}; t).$$

By using the dipole approximation and length gauge [$\hat{U}_{\text{int}}(t) = \vec{r} \cdot \vec{E}(t)$], next to the analytical form of the Volkov states $\Psi_V(\vec{k}, \vec{r}; t) = \exp\{-\frac{i}{2} \int_0^t [\vec{k} + \vec{A}(t')]^2 dt' + i[\vec{k} + \vec{A}(t)] \cdot \vec{r}\}$, a final

expression (coupled-differential equations, identical to the **TDSE**) for the $c(\vec{k}; t)$ coefficients can be analytically deduced:

$$\frac{\partial c(\vec{k}; t)}{\partial t} = \frac{\exp\{\frac{i}{2}[k^2 t + 2\vec{k}\vec{F}(t)]\}}{i(2\pi)^3} \int d\vec{k}' c(\vec{k}'; t) \exp\left\{\frac{-i}{2}[k'^2 t + 2\vec{k}'\vec{F}(t)]\right\} \int d\vec{r} V(\vec{r}) e^{i(\vec{k}' - \vec{k}) \cdot \vec{r}},$$

where $\vec{F}(t) = \int_0^t dt' \vec{A}(t')$, while the last term represents the Fourier-transform of the Coulomb-potential [in the case of the H atom ($V = -1/r$) this equals to $\mathcal{F}(\vec{k}', \vec{k}) = -4\pi/(\vec{k}' - \vec{k})^2$]. The expansion coefficient (i.e., the time-dependent wave function) can be obtained by solving the coupled-differential equation directly (**TDSE model**) [46] with the use of some differential-equation-solving algorithm (e.g., fourth-order Runge-Kutta methods) or iteratively (**iTDSE model**) [47]:

$$c^{(n)}(\vec{k}; t) = c^{(n)}(\vec{k}; t_s) + \int_{t_s}^t dt' \frac{\exp\{\frac{i}{2}[k^2 t' + 2\vec{k}\vec{F}(t')]\}}{i(2\pi)^3} \int d\vec{k}' c^{(n-1)}(\vec{k}'; t') e^{\frac{-i}{2}[k'^2 t' + 2\vec{k}'\vec{F}(t')]} \mathcal{F}(\vec{k}, \vec{k}'),$$

where n represents the order of iteration [within the *momentum-space strong field approximation* (**MSSFA**) model $n = 1$], and where it was considered that $c^{(n-1)}(\vec{k}'; t) \simeq c^{(n-1)}(\vec{k}'; t_s)$ is time invariant between t_s and t . The methods were compared for the H atom irradiated with

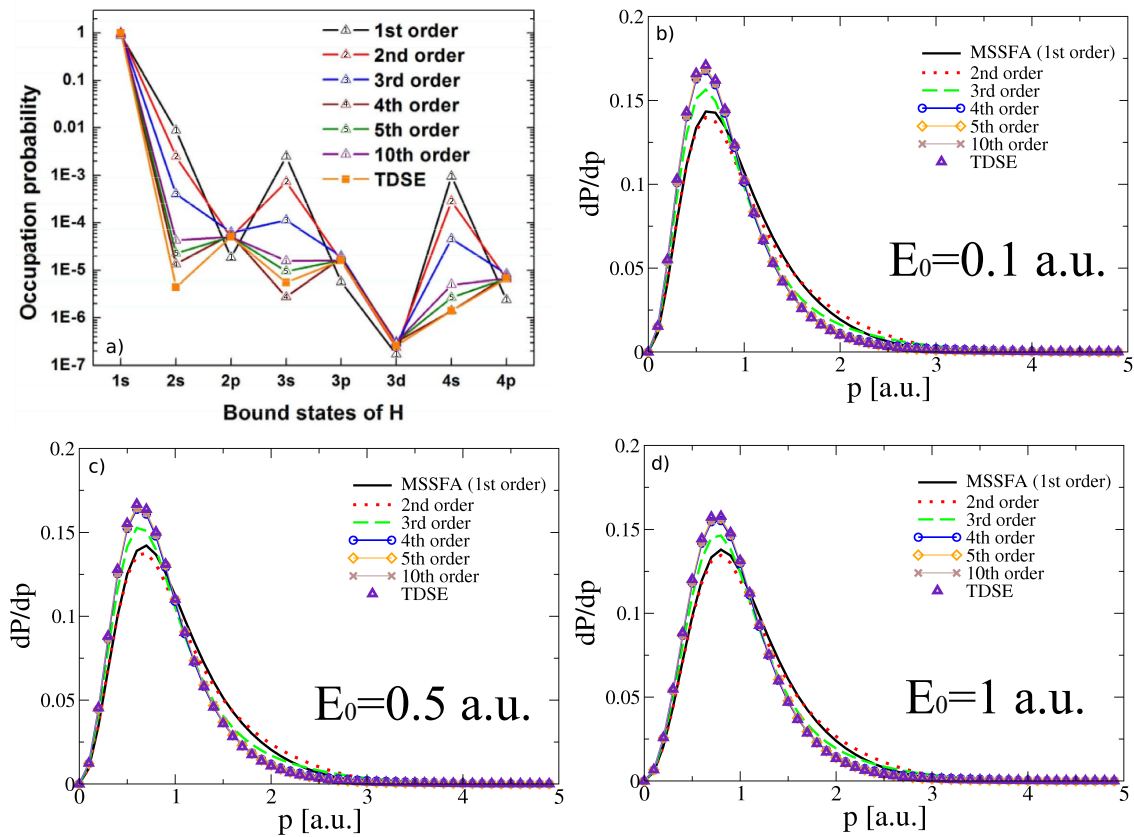


Figure 2.2: The occupation probability of different electronic bound states calculated at $t = \tau$ (a); the ejected electron spectra as a function of electron momentum ($\vec{k} \rightarrow \vec{p}$) for different field amplitudes (laser intensities): (b) $E_0 = 0.1$ a.u.; (c) $E_0 = 0.5$ a.u.; (d) $E_0 = 1$ a.u..

a half-cycle laser pulse [$E(t) = E_0 \sin(\omega t + \varphi_0) \sin^2(\frac{\pi t}{\tau})$]; where $\tau = 5$ a.u. is the duration of the pulse, $\omega = 0.05$ a.u., $\phi_0 = -\omega\tau/2 - \pi/2$], by comparing the obtained photoelectron spectra (see Fig. 2.2) calculated as:

$$\frac{dP}{d\vec{k}}(\vec{k}) = |\langle \psi_{\vec{k}}(\vec{r}) | \Psi(\vec{r}; t) \rangle|^2,$$

where for the continuum $\psi_{\vec{k}}(\vec{r})$ states, first the plane waves were used (*TDSE-O* model) after the bound states were subtracted from the WF (by using the Gram-Schmidt orthogonalization procedure); second, the exact (one-center Coulomb) continuum states were also used (*TDSE-C* model). It can be seen, that the iterative method approached the results obtained by the exact (direct solution of the TDSE) model, from which one may conclude that the iTDSE model can be used as an alternative and also reliable tool to investigate laser induced electron dynamics.

2.2 TDSE for diatomic molecules

In the present work the time evolution of the laser irradiated molecular system is studied within the framework of the frozen core approximation (i.e., the positions of the nuclei are fixed). This approximation is reliable due to the fact, that throughout this work high intensity ($\geq 10^{16}$ Wcm $^{-2}$) few-cycle XUV laser pulses are considered, resulting in ultrashort interaction times (few tens of attoseconds), which are significantly shorter than the timescale of the nuclear motions (vibration, rotation). During this time interval the motion of the nuclei can be considered negligible next to the rapid movement of the electrons, thus the induced nuclear dynamics can be neglected (the effect of the nuclear dynamics becomes more significant in the case of longer, multi-cycle laser pulses). Nevertheless, because the goal of this work was to calculate the interference map of the ejected EWPs, and to correctly understand the physics behind it, we restricted ourselves only to few-cycle (two cycles in the present case) XUV pulses. Considering these field parameters, the use of the frozen core approximation is well founded.

Starting from the Born-Oppenheimer approximation the molecular wave function is written as the product of the electronic (Ψ) and the nuclear wave function (χ):

$$\Psi_{\text{mol}} = \Psi_{\{\vec{R}\}}(\vec{r}; t) \chi(\vec{R}; t),$$

with \vec{r} being the position of the active electron, and \vec{R} representing the nuclear coordinates (i.e., internuclear distance). Considering this, the TDSE for the active electron is given as:

$$i\hbar\partial_t\Psi(\vec{r}; t) = \hat{H}(t)\Psi(\vec{r}; t) = [\hat{H}_0 + \hat{U}_{\text{int}}(t)]\Psi(\vec{r}; t), \quad (2.1)$$

where $\hat{H}(t)$ is the electronic Hamiltonian, $\hat{H}_0 = \hat{T} + \hat{V}$ is the field-free part, which is given as the sum of the kinetic-energy and the Coulomb potential term, while $\hat{U}_{\text{int}}(t) = \vec{r} \cdot \vec{E}(t)$ is

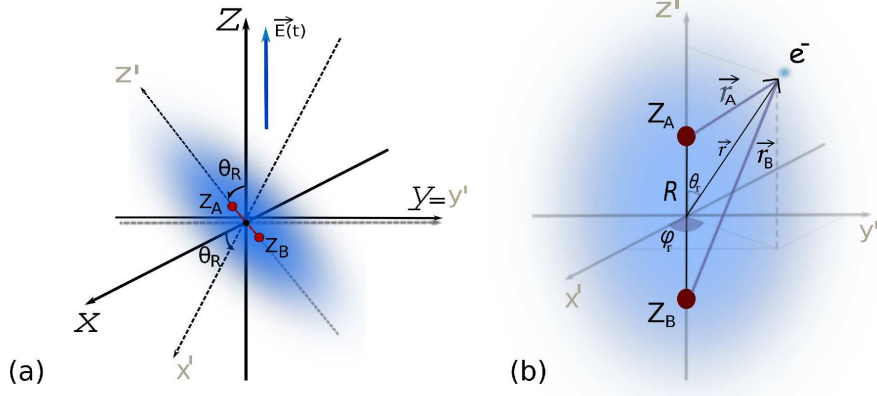


Figure 2.3: The molecular orientation with respect to the laser field (a) and the molecular framework (b).

the laser-electron interaction contribution. The notation $\partial_t = \partial/\partial t$ was used. By using the prolate spheroidal coordinates

$$\xi = (r_A + r_B)/R; \quad \eta = (r_A - r_B)/R; \quad \varphi \text{ (the azimuthal angle)}, \quad (2.2)$$

and the following analytical forms of the Hamiltonian operator's different contributions:

$$\begin{aligned} \hat{T} &= -(\nabla^2/2m_e) = \frac{2}{m_e R^2} \left[\frac{\hat{T}_\xi + \hat{T}_\eta}{J(\xi, \eta)} - \frac{\partial_\varphi^2}{(\xi^2 - 1)(1 - \eta^2)} \right], \text{ with} \\ \hat{T}_\xi &= -(d/d\xi)(\xi^2 - 1)(d/d\xi); \quad \hat{T}_\eta = -(d/d\eta)(1 - \eta^2)(d/d\eta); \quad J(\xi, \eta) = \xi^2 - \eta^2; \\ \hat{V} &= -(2/R)[Z_A(\xi - \eta) + Z_B(\xi + \eta)]J^{-1}(\xi, \eta); \\ \hat{U}_{\text{int}}(t) &= \vec{r} \cdot \vec{E}(t) = E(t)z = (R/2)E(t)[\xi\eta \cos \theta_R + \sqrt{(\xi^2 - 1)(1 - \eta^2)} \sin \theta_R]; \end{aligned}$$

next to the following *ansatz* of the the wave function

$$\Psi(\vec{r}; t) = \sum_{m=-\infty}^{\infty} \Psi^{(m)}(\xi, \eta; t) e^{im\varphi} / \sqrt{2\pi}, \quad (m \in \mathbb{Z}),$$

the **TDSE in prolate spheroidal coordinate** system reads as:

$$\begin{aligned} i\partial_t \Psi^{(m)}(\xi, \eta; t) &= [\hat{T}^{(m)} + \hat{V}] \Psi^{(m)}(\xi, \eta; t) + (R/2)E(t)\xi\eta \cos \theta_R \Psi^{(m)}(\xi, \eta; t) + \\ &+ (R/2)E(t)\sqrt{(\xi^2 - 1)(1 - \eta^2)} \sin \theta_R [\Psi^{(m-1)}(\xi, \eta; t) + \Psi^{(m+1)}(\xi, \eta; t)]/2. \end{aligned}$$

Here for calculating the expression of $\hat{T}^{(m)}$ the property $\partial_\varphi^2 \Psi = -m^2 \Psi$ was used, and θ_R was the angle between the internuclear axis ($0z'$) and the electric vector component of the linearly polarized laser field. $r_{A,B}$ represented the distances measured from the the two nuclei having the electrical charges $Z_{A,B}$.

Numerical discretization: the Finite Element Discrete Variable Representation grid

For the discretization of the $\Psi^{(m)}(\xi, \eta)$ the finite element discrete variable representation (FE-DVR) method was used for both coordinate axis. According to the FE-DVR method the configuration space ($\xi \in [1, \xi_{\max}]$; $\eta \in [-1, 1]$) was divided into smaller sub-domains (finite elements, FEs), and the WF expanded in the basis of DVR functions that were local to each α -th FE. In each FE N_{fun} number of DVR basis functions were used, which were defined as:

$$f_p^{(\alpha)}(x) = \begin{cases} [L_1^{(\alpha)}(x) + L_{N_{\text{fun}}}^{(\alpha-1)}(x)] (w_1^{(\alpha)} + w_{N_{\text{fun}}}^{(\alpha-1)})^{-1/2}, & p = 1; \\ L_p^{(\alpha)}(x) (w_p^{(\alpha)})^{-1/2}, & p = 2, \dots, N_{\text{fun}} - 1; \\ [L_{N_{\text{fun}}}^{(\alpha)}(x) + L_1^{(\alpha+1)}(x)] (w_{N_{\text{fun}}}^{(\alpha)} + w_1^{(\alpha+1)})^{-1/2}, & p = N_{\text{fun}}, \quad \text{where} \end{cases} \quad (2.3)$$

$$L_p^{(\alpha)}(x) = \mathcal{P}_p^{(\alpha)}(x)\theta(x - x_1^{(\alpha)})\theta(x_{N_{\text{fun}}}^{(\alpha)} - x); \quad \text{and} \quad \mathcal{P}_p(x) = \prod_{k \neq p}^{N_{\text{fun}}} \frac{x - x_k}{x_p - x_k}.$$

Since the Hamiltonian contains at most second order derivatives it is sufficient to ensure the continuity at the finite element boundaries, which was achieved by the use of the so-called "bridge" functions (i.e., the basis functions when $p = 1, N_{\text{fun}}$). The $\mathcal{P}_p(x)$ are the Lagrange interpolating polynomials with the property $\mathcal{P}_p(x_q) = \delta_{pq}$, while $\theta(x)$ is the Heaviside step function: $\theta(x - x_0) = 1$ if $x \geq x_0$; 0 if $x < x_0$. In each FE the Lagrange interpolating polynomials were defined using a set of local gridpoints - the Gauss-Lobatto quadrature points - with $w_p^{(\alpha)}$ being their associated weights. By using the global indexing $i \equiv (\alpha^{\{\xi\}}, p^{\{\xi\}})$ and $j \equiv (\alpha^{\{\eta\}}, p^{\{\eta\}})$ for the local ξ and η gridpoints, and by denoting with $f_i(\xi)$ and $g_j(\eta)$ the two set of basis functions, the WF was expanded as:

$$\Psi^{(m)}(\xi, \eta; t) = \sum_{i'=1}^{N_\xi} \sum_{j'=1}^{N_\eta} \psi_{i'j'}^{(m)}(t) f_{i'}(\xi) g_{j'}(\eta) / \sqrt{(R^3/8)J(\xi_{i'}, \eta_{j'})}, \quad (2.4)$$

and the TDSE in prolate spheroidal coordinates on the defined FE-DVR grids written as:

$$\begin{aligned} i\partial_t \psi_{ij}^{(m)}(t) &= \sum_{i',j'} \left\{ (2/m_e R^2) J_{ij}^{-1/2} J_{i'j'}^{-1/2} [\delta_{jj'} \langle f_i | \hat{T}_\xi | f_{i'} \rangle + \delta_{ii'} \langle g_j | \hat{T}_\eta | g_{j'} \rangle] \right. \\ &+ \delta_{ii'} \delta_{jj'} [(2m^2 / (m_e R^2 (\xi_i^2 - 1)(1 - \eta_j^2)) + V_{ij} + E(t) z'_{ij} \cos \theta_R] \left. \right\} \psi_{i'j'}^{(m)}(t) + \\ &+ \sum_{i',j'} \left\{ \delta_{ii'} \delta_{jj'} E(t) x'_{ij\{\varphi=0\}} \sin \theta_R \right\} (\psi_{i'j'}^{(m-1)}(t) + \psi_{i'j'}^{(m+1)}(t)) / 2, \end{aligned}$$

where $z'_{ij} = (R/2)\xi_j\eta_j$, and $x'_{ij\{\varphi=0\}} = (R/2)(\xi_i^2 - 1)^{1/2}(1 - \eta_j^2)^{1/2}$. (2.5)

TDSE in symmetrical matrix form

In order to obtain physically accurate results the $\hat{H}(t)$ operator should be represented

by a Hermitian matrix. By taking into account that in the expansion of the $\Psi^{(m)}(\xi, \eta; t)$ the $f_i(\xi)$ and $g_j(\eta)$ basis functions are real, the Hamiltonian matrix should be symmetrical. The matrix elements of the Coulomb interaction operator (V_{ij}) and the laser-interaction operators are symmetrical (diagonal matrices), but the kinetic-energy matrix should have been symmetrized. The symmetrization was achieved by integrating by parts the $(\hat{T}_\eta)_{jj'}$, $(\hat{T}_\xi)_{ii'}$ elements:

$$\langle g_j | \hat{T}_\eta | g_{j'} \rangle = - \int_{-1}^1 d\eta g_j(\eta) \frac{d}{d\eta} \left[(1-\eta^2) \frac{d}{d\eta} g_{j'}(\eta) \right] = - \left[(1-\eta^2) g_j g_{j'}' \right] \Big|_{-1}^{+1} + \int_{-1}^1 d\eta (1-\eta^2) g_j' g_{j'}'$$

$$\langle f_i | \hat{T}_\xi | f_{i'} \rangle = - \int_1^\infty d\xi f_i(\xi) \frac{d}{d\xi} \left[(\xi^2-1) \frac{d}{d\xi} f_{i'}(\xi) \right] = - \left[(\xi^2-1) f_i f_{i'}' \right] \Big|_1^\infty + \int_1^\infty d\xi (\xi^2-1) f_i' f_{i'}'$$

In the above equations only the last (symmetric) terms remain, since when $\eta = \pm 1$ the term $1-\eta^2$ vanishes; while for $\xi = 1$ the term ξ^2-1 is zero and the equality $\lim_{\xi \rightarrow \infty} f_i^{(\text{Last FE})}(\xi) = 0$ can be safely considered, since the value infinity lies outside of the last FE on the truncated FE-DVR grid. According to the above considerations a symmetric Hamiltonian was obtained by applying the Gauss integration quadratures to evaluate the remaining integrals:

$$(\hat{T}_\eta)_{jj'} \simeq \sum_l \tilde{w}_l (1-\eta_l^2) g_j'(\eta_l) g_{j'}'(\eta_l); \quad (\hat{T}_\xi)_{ii'} \simeq \sum_k w_k (\xi_k^2-1) f_i'(\xi_k) f_{i'}'(\xi_k). \quad (2.6)$$

In both expressions above the first order derivation of the interpolating functions were involved: $\partial_x L_p^{(\alpha)}(x) = \partial_x \mathcal{P}_p^{(\alpha)}(x) \theta(x - x_1^{(\alpha)}) \theta(x_{N_{\text{fun}}}^{(\alpha)} - x) + D_{\text{diff}}(x)$, where a diffusion term appeared $D_{\text{diff}}(x) = \mathcal{P}_p^{(\alpha)}(x) [\theta(x_{N_{\text{fun}}}^{(\alpha)} - x) \delta(x - x_1^{(\alpha)}) - \theta(x - x_1^{(\alpha)}) \delta(x_{N_{\text{fun}}}^{(\alpha)} - x)]$ with the Dirac-delta functions: $\delta(x - x_0)$. Using the matrix formalism the wave function labelled with the quantum number m can be given in the form of a column matrix:

$$|\psi^{(m)}(\xi, \eta)\rangle \rightarrow \left[\psi^{(m)}(\eta_1, \xi_1), \psi^{(m)}(\eta_2, \xi_1), \dots, \psi^{(m)}(\eta_{N_\eta}, \xi_1), \psi^{(m)}(\eta_1, \xi_2), \dots, \psi^{(m)}(\eta_{N_\eta}, \xi_{N_\xi}) \right]^T;$$

and the Hamiltonian as a sparse $(N_\xi \times N_\eta)^2$ sized matrix with a large portion of off-diagonal zero valued regions (where N_ξ and N_η are the total number of considered gridpoints on each coordinate axis).

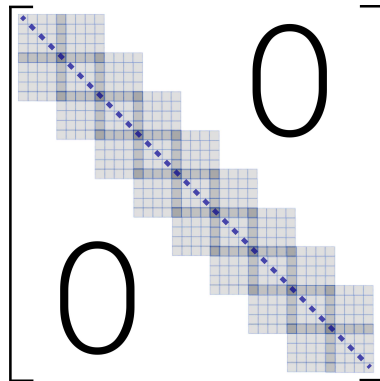


Figure 2.4: The shape of the kinetic energy parts - (\hat{T}_ξ) , (\hat{T}_η) matrices - of the Hamiltonian.

Numerical implementation and integration of the TDSE

Since large off-diagonal regions of the Hamiltonian had zero values, from the numerical point of view the matrix-vector multiplications became cheap. Moreover, a further optimization of the calculations was achieved by employing a proper parallelization (OpenMPI) along the ξ configuration space (i.e., the same number of FEs were distributed on each CPU). In the present work, the orientation of the molecular axis was constrained parallel to the laser field polarization vector ($\theta_R = 0$), which significantly reduced the numerical complexity of the studied system. Hence, due to the cylindrical symmetry around the molecule, the coupling (i.e., the population transfer) between the partial channels corresponding to different m values disappeared, and since the simulation was started from an $m=0$ state (the $1s\sigma_g$ ground state obtained by the direct diagonalization of the field-free Hamiltonian by using the SLEPc package [48]) the dimensionality of the original 3D problem was reduced to 2D.

Then this initial state was propagated in time by using the short-iterative Lanczos (SIL) scheme [49], in the framework of which a $N_K = n + 1$ dimensional Krylov-subspace [50] was constructed - in each time step - by the repeated action of the Hamiltonian on the $|\Psi_0\rangle = |\Psi(\vec{r}; t)\rangle$ state as follows:

$$K_n(t) = \left\{ |\Psi_0\rangle, \hat{\mathbf{H}}|\Psi_0\rangle, \hat{\mathbf{H}}^2|\Psi_0\rangle, \dots, \hat{\mathbf{H}}^n|\Psi_0\rangle \right\}; \quad (2.7)$$

which in turn was transformed into an orthonormal set of $|q_i\rangle$ vectors ($\langle q_i|q_j\rangle = \delta_{ij}$) by using the Gram-Schmidt procedure. Finally the wave function was calculated as

$$|\Psi(\vec{r}; t + \delta t)\rangle = \hat{U}(t + \delta t, t)|\Psi(\vec{r}; t)\rangle = \sum_{k=0}^n \sum_{j=1}^{n+1} \Phi_{k+1}(j) e^{-i\epsilon_j \delta t} \Phi_1(j) |q_k\rangle, \quad (2.8)$$

where the approximation $\hat{U} \simeq \hat{U}^Q = \exp\{-i\hat{\mathbf{H}}^Q(t)\delta t\} = \mathbf{Q} \exp\{-i\hat{\mathbf{h}}\delta t\}\mathbf{Q}^\dagger$ of the evolution operator was used, and the $\{\Phi_k, \epsilon_k\}$ were the eigenvectors and eigenvalues of the newly constructed (\hat{h}) Hamiltonian matrix, the elements of which were calculated as $\mathbf{h}_{ij} = \langle q_i|\hat{\mathbf{H}}|q_j\rangle$. The convergence of the time-propagation step was achieved by fixing the $\Delta t \rightarrow \delta t$ and increasing appropriately N_K .

Calculating physical quantities: Photoelectron spectrum

By employing the aforementioned temporal propagation scheme the $\Psi(\vec{r}; t) \rightarrow \Psi(\xi, \eta; t)$ WF was obtained (with $\langle \Psi|\Psi\rangle = 1$), and was used to calculate physical observables, such as the expected position of the ionized electron: $\bar{r}(t) = \langle \Psi_{\text{free}}|r|\Psi_{\text{free}}\rangle / \langle \Psi_{\text{free}}|\Psi_{\text{free}}\rangle$; and in the final stage the ionization probability density [i.e., photoelectron spectrum (PES)]:

$$\frac{dP}{dk}(k; \theta_k; t) = |\langle \Psi_{\vec{k}}|\Psi_{\text{free}}(t)\rangle|^2, \quad (2.9)$$

where for the exact $|\Psi_{\vec{k}}\rangle$ continuum states the approximate $|\Psi_C\rangle$ one-center Coulomb func-

tions were used, and the $|\Psi_{\text{free}}(t)\rangle$ free part of the WF was obtained by subtracting the $|\varphi_b\rangle$ bound states from the wave function: $|\Psi_{\text{free}}\rangle = |\Psi\rangle - \langle\varphi_b|\Psi\rangle|\varphi_b\rangle$; because these states were not orthogonal to the approximate continuum states. In order to eliminate further errors that the one-center Coulomb functions would have brought into the image of the PES, the WF was further propagated in time - after the completion of the pulse ($t > \tau$) -, until the low momentum electrons had also left the very near regions of the nuclei (those regions where the difference between the one-center Coulomb function and the exact one is the largest), and reached those far regions, where the differences between these two could be safely considered negligible.

3. Results and discussion

3.1 Convergent bound state wave functions and bound state energies of H_2^+

In the very first step convergence tests were carried out in order to obtain the optimal numerical (spatial) discretization parameters (ξ_{\max} , $\Delta\xi$, $\Delta\eta$) and the accurate/convergent bound state wave functions and bound state energies of the H_2^+ molecule [51]. This was achieved by diagonalizing the $H(0)$ field-free Hamiltonian with the use of the Scalable Library for Eigenvalue Problem Computations (SLEPc) package [48]. The symmetries of each bound

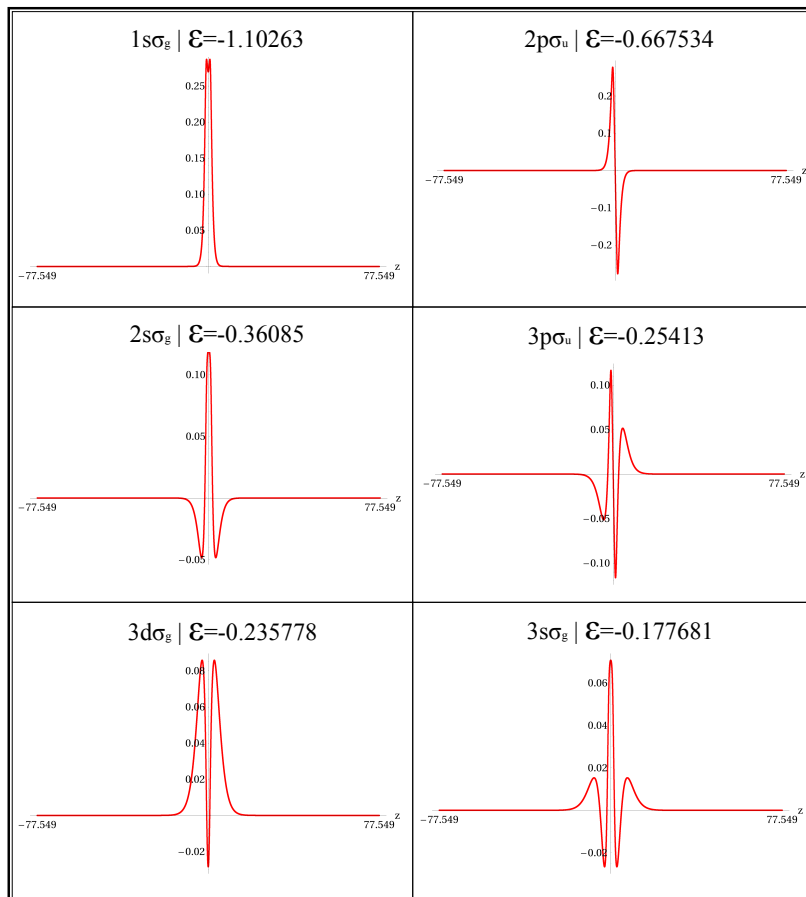


Figure 3.1: The first six electronic bound states' wave function and bound energies of the H_2^+ molecule obtained by diagonalizing the field-free Hamiltonian for the equilibrium internuclear separation $R = 2$ a.u.. The plots show the $\varphi_i(\vec{r})$ wave functions rotated into the real plane. state was identified numerically by counting the nodal planes in both ξ and η directions. Moreover, the bound $\varphi_j^{\{R\}}$ wave functions were calculated for a large number of R internuclear distances, and the obtained $\varepsilon_j(R)$ eigenenergies of $\hat{H}(0)$ were added to the proton-proton repulsion energy $1/R$, and then the obtained potential energy curve (PEC) $[\varepsilon_j(R) + 1/R]$ plotted next to data found in the literature [52]:

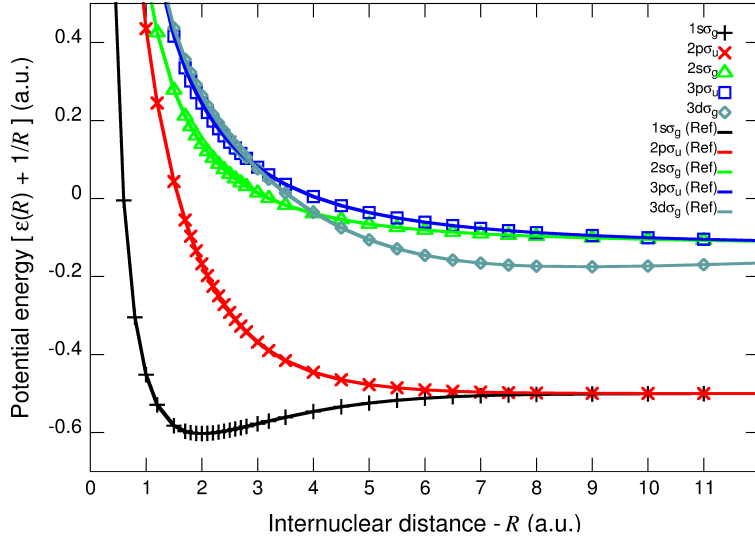


Figure 3.2: The calculated potential energy curves (PECs) for different BSs plotted next to the reference data (solid lines) [52]. The equilibrium distance is located at the lowest energy $1s\sigma_g$ (ground) state when $R_0 = 2$ a.u.. The higher energy states are dissociative states.

3.2 XUV-field induced electron dynamics: Photoexcitation of H_2^+

In the present case, where the main and final goal was to investigate the physics behind the creation of the holographic image of the H_2^+ molecule created with photoelectrons, it was more appropriate to restrict the calculations to laser pulses having shorter wavelengths, i.e., by considering high frequency XUV radiations. This statement holds, since in the case when larger wavelengths are used also the periods of the laser fields are longer, hence more EWPs are emitted in the continuum on different time moments of the same optical half-cycle, which on the other hand will result in a rather complex (difficult to be deciphered) electron trajectory mechanism and interference patterns. In accordance with this, a two-cycle laser field with frequency $\omega_{\text{XUV}} = 0.4445$ a.u. was chosen from the XUV regime [ω corresponds to a $\lambda \approx 100$ nm ($\nu = 2.92$ PHz = 2.92×10^{15} s $^{-1}$) central wavelength radiation], where the pulse duration was fixed to $\tau = 28.26$ a.u., and $\varphi_{\text{CEP}} = -(\omega\tau + \pi)/2$, which resulted a symmetric pulse in time. In order to obtain relevant information regarding how the value of the internuclear distance (R) influences the photoelectron hologram, three different $R \in \{1, 2, 4\}$ a.u. configurations were investigated, which were illuminated with different field intensities ($E_0 \in \{0.25, 0.5, 0.75, 1\}$ a.u.), such that the Keldysh-gamma parameter was kept in the vicinity of 1 (not far from the transition region between the tunneling and above threshold ionization). For all the considered R values the similar behavior of the BSs' occupation probabilities (OPs) was observed [53]: (i) the major dynamics (the considerable depletion of the ground next to the rapid increase of the $2p\sigma_u$ state's OP) occurred at the first major maximum of the field (i.e., $t = \tau/4 \simeq 7$ a.u.); (ii) and at the the central maximum ($t = \tau/2 \simeq 14$ a.u.), which almost totally emptied the low-lying bound states; (iii) a small, but not negligible amount of OPs were detectable after the completion of the laser pulse

($t > \tau$). The dynamics of the OPs were found to be in accordance with the selection rules of optical transitions, where it was shown that for the case of low field intensities (when $t < \tau/5$) the $1s\sigma_g \rightarrow 2p\sigma_u$ transition (being realized by absorbing an odd - at least 1 - number of photons) was more pronounced than the $1s\sigma_g \rightarrow 2s\sigma_g$ excitation (needs an even number of absorbed photons, minimum 2). For the first part of the pulse ($t < \tau/2$), the OPs of the $2s\sigma_g$ and $3p\sigma_u$ showed more or less the similar trend, which can be explained by the fact that a balance was achieved in the dynamics of $1s\sigma_g \rightarrow 2s\sigma_g$ and $1s\sigma_g \rightarrow 3p\sigma_u$ transitions.

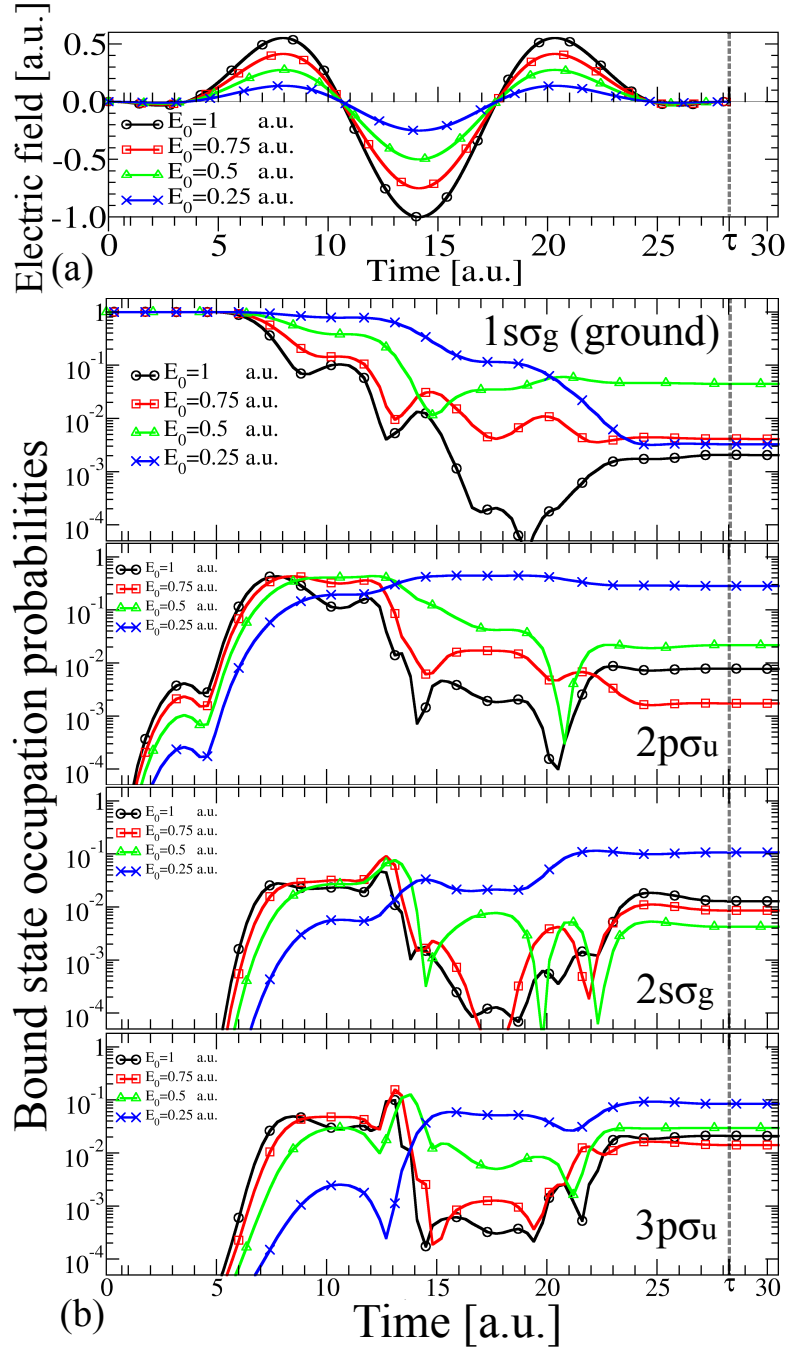


Figure 3.3: (a) The temporal shape of the laser's electric field component for different E_0 field amplitudes. (b) The occupation probabilities of the first 4 bound states as a function of time for different electric field amplitudes and for the fixed internuclear distance $R = 2$ a.u..

3.3 The ionization of H_2^+ : Obtaining convergent photoelectron spectra

Since the scattering states used during the calculation of the PES - as already stated earlier - were approximate ones, the obtained PESs contained a certain amount of error. However the introduced errors could be reduced by further propagating the WF after the conclusion of the laser pulse, and by subtracting the contributions of the BSs (which were shown to be present in the excitation processes after $t = \tau$) from the WF prior to the calculation of the final spectra. In order to show this error can be reduced to minimal, first, investigation regarding on how the number of the subtracted BSs influences the PES, second, how these spectra depend on the propagation time after $t > \tau$. Convergence tests for all considered internuclear distances were carried out, and the convergence behavior of the PESs was found to be similar for all R values. Here the results for $R = 4$ a.u. are concisely presented.

Convergence of the bound state subtraction

At time moment 5τ (measured from the start of the laser pulse) the PESs were calculated for cases when a different number of BSs were removed from the TDWF. In Fig. 3.4 the spectra obtained for the internuclear separation $R = 4$ a.u. and for different number of removed bound states (N_{BS}) are shown. The concentric rings observable in Fig. 3.4(a) are the direct consequence of the non-orthogonality of the H_2^+ BSs with respect to the used approximate scattering states. The projection of the bound part of the wave function onto single center Coulomb wave functions is non-vanishing, and during the calculation of the PES it was coherently added to the projection of the continuum part of the TDWF leading to the concentric ring structure observed. With gradual subtraction of the BSs the concentric rings started to fade away: For $N_{\text{BS}} = 5$ they are already significantly reduced [Fig. 3.4(b)], while for $N_{\text{BS}} \geq 20$ they are barely visible.

This behavior was also visible when the PES as a function of electron ejection angle (measured from the polarization vector of the laser field) was plotted for fixed electron momentum values. For $k = 0.5$ a.u. a significant change in the spectra was observed as N_{BS} was increased from 0 to 5, and then to 20, while for $N_{\text{BS}} \geq 20$ the changes in the PESs were

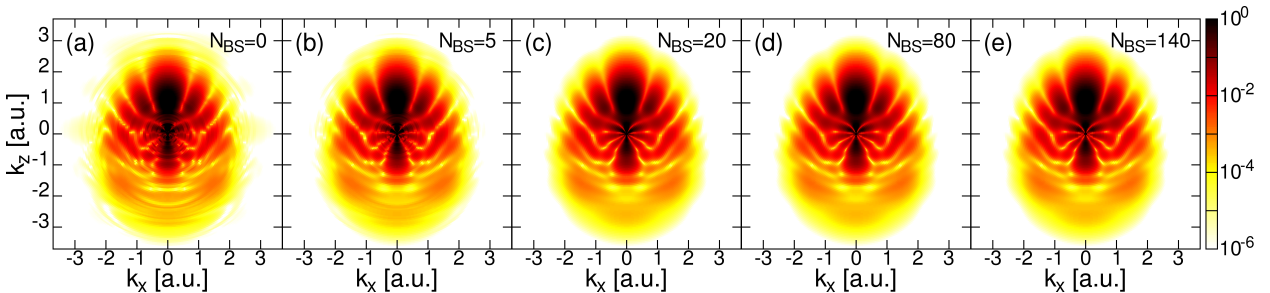


Figure 3.4: Photoelectron spectra calculated as a function of number of subtracted bound states (N_{BS}) considered at time moment 5τ for the internuclear separation $R = 4$ a.u.. (a) $N_{\text{BS}} = 0$; (b) $N_{\text{BS}} = 5$; (c) $N_{\text{BS}} = 20$; (d) $N_{\text{BS}} = 80$; (e) $N_{\text{BS}} = 140$.

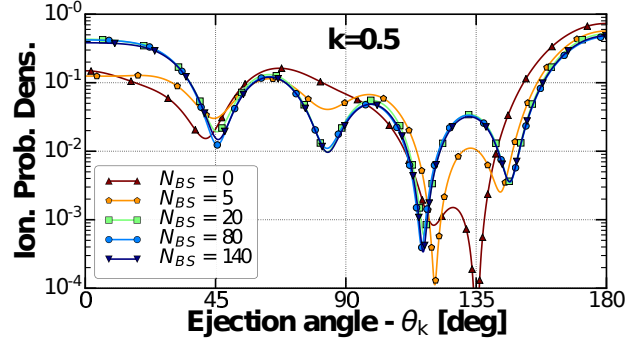


Figure 3.5: Ionization probability density at $t = 5\tau$ for the fixed $k = 0.5$ a.u. momentum as a function of subtracted bound states number for $R=4$ a.u..

negligible. After analyzing the spectrum at different fixed electron momentum values - by scanning both the lower and higher momentum part - no significant differences between the results obtained for $N_{\text{BS}} \geq 20$ were observed. Similar convergence tests showed the similar behavior for the other R internuclear distances, with the remark that with the decrease of R (increase of I_p) the number of subtracted states required for a converged PES increased, because for smaller R values a larger portion of the WF was distributed among the BSs. Hence, in order to eliminate as much as possible the undesired errors the BSs would bring into the PES image a total number of $N_{\text{BS}} = 120$ bound state subtraction was considered.

Convergence as a function of propagation time

The image of the PES for different time moments after the completion of the laser pulse was studied. In Fig. 3.6 the PESs obtained for $R = 4$ a.u. at $t = \tau$, 3τ , and 5τ are shown. A noticeable change in the image of spectra as a function of the propagation time was observed for small photoelectron momentum values ($k \leq 1$ a.u.). In contrast, for the high electron momentum values the changes in the spectra with increasing propagation time were barely observable. This convergence behavior can be understood based on simple arguments. The difference between the simple one-center Coulomb wave functions and the exact scattering states of the H_2^+ target is the largest in the immediate vicinity of the target. Thus, when the spectrum of the continuum EWPs were calculated, the projection error introduced by

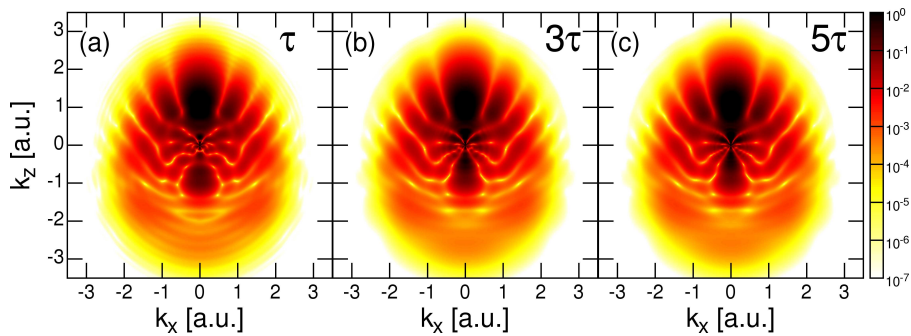


Figure 3.6: Ionization probability density calculated for the internuclear distance $R = 4$ a.u. as a function of electron momentum component perpendicular (k_x) and parallel (k_z) to the laser polarization vector calculated at time moments: (a) τ ; (b) 3τ ; (c) 5τ .

the approximate scattering states was larger if the continuum EWPs were closer to the target. With the increase of the propagation time the projection error decreased, which can be explained by the fact that with increasing the propagation time the continuum EWPs departed from the vicinity of the target and arrived to the regions of the coordinate space, where the difference between the exact and approximate scattering states is smaller. The low momentum part of the continuum EWP departs much slower from the vicinity of the target, thus as it is observed on Fig. 3.6 the low momentum part of PES (compared to the high momentum part) was more severely impacted by the projection error. The above outlined arguments are also supported by the fact, that with increasing propagation time the changes in the PES are smaller: while the difference between the PESs calculated at $t = 1\tau$ and $t = 3\tau$ time moments are clearly identifiable, until then the differences between the $t = 3\tau$ and $t = 5\tau$ PESs are less obvious.

In addition to that, more rigorous investigations were made by taking cuts along fixed $|\vec{k}|$ and θ_k (ejection angle) values. In each cases, a faster convergence for the larger k values was observed, which is supported by the fact that the electrons with larger momenta (i.e., higher velocities) are further away from the two nuclei than those with smaller momenta.

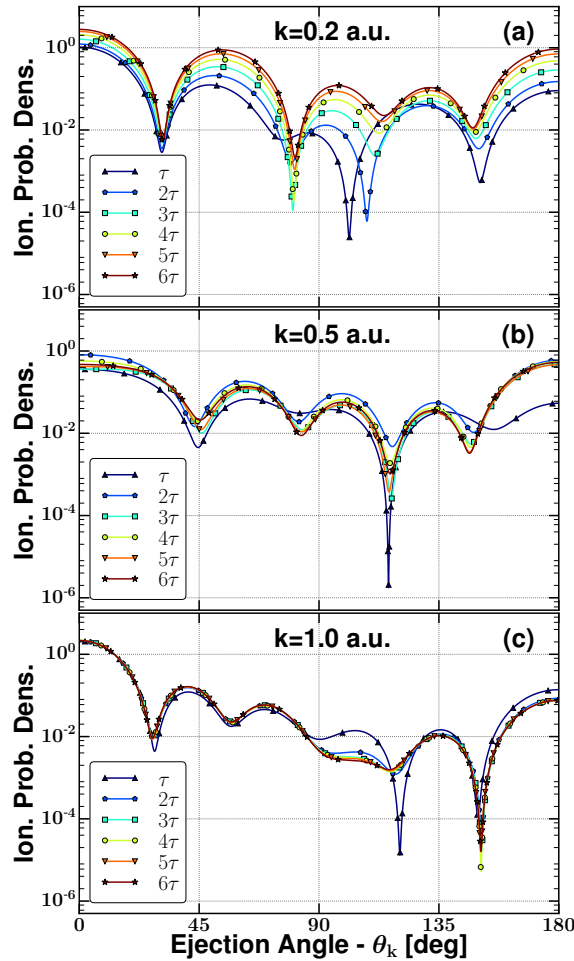


Figure 3.7: The angular distribution of photoelectrons as a function of the propagation time. Results are shown for $R = 4$ a.u. and for different electron momentum values: $k=0.2$ a.u. (a); $k=0.5$ a.u. (b); $k=1$ a.u. (c).

Convergence parameter assigned to the calculated PES

A “full” convergence (also for small k values) can be achieved by propagating the WF even further in time. However, for those calculations the coordinate space simulation box should also be increased (to prevent absorption and reflection at the simulation box boundary), which would imply a non-negligible increase of the CPU time required for the simulations. In order to quantitatively describe the convergence of the spectra the

$$\mathcal{E}(t) = \frac{\int \int dk_x dk_z |P(k_x, k_z; t) - P(k_x, k_z; \tau)|}{\int \int dk_x dk_z P(k_x, k_z; \tau)} \quad (\text{for } t > \tau) \quad (3.1)$$

quantity was introduced, which measures the relative difference between the PES calculated at the end of the laser pulse ($t = \tau$) and the spectra calculated at a later time moment $t > \tau$. It was observed for all R cases that $\mathcal{E}^R(t)$ exponentially converged towards an asymptotic value \mathcal{E}_∞^R , which was obtained by fitting the calculated $\mathcal{E}^R(t)$ data points with the function $\mathcal{E}_{\text{fit}}^R(t) = \mathcal{E}_\infty^R - \beta e^{-\alpha t}$ ($\alpha, \beta \in \mathbb{R}^+$), and the relative error of the PES was estimated as:

$$\delta_{\text{conv}}^R(t) = \mathcal{E}_\infty^R - \mathcal{E}^R(t). \quad (3.2)$$

In Fig. 3.8 this error estimate was plotted as a function of time along with its exponential fit ($\beta e^{-\alpha t}$) for different R values. For each internuclear separation $\delta_{\text{conv}}^R(t)$ showed an excellent agreement with the used exponential fit confirming the assumed exponential decrease of the projection error. As it is indicated on Fig. 3.8, for the propagation time 5τ the error estimate for each internuclear distance is below 0.5%. Since this remaining error is affecting only the low momentum part of the PES, and the dominant features of the photoelectron hologram are located at the high momentum part of the spectrum, for the results presented in the following, the time propagation was ended at $t = 5\tau$.

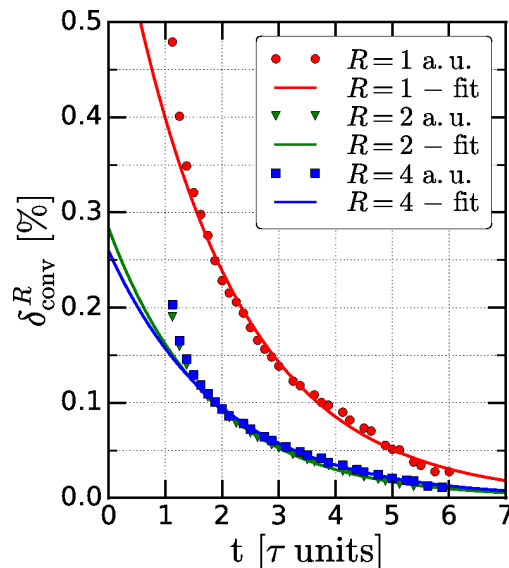


Figure 3.8: The error estimate δ_{conv}^R as a function of time for different R values. The data points are shown along with the $\beta e^{-\alpha t}$ fit.

3.4 The effect of the laser field intensity on the photoelectron hologram

By fixing the frequency of the radiation field to $\omega = 0.4445$ a.u., the duration of the laser pulse to $\tau = 28.26$ a.u., and modifying the value of the electric field's amplitude (E_0) the ionization of the H_2^+ was investigated. Here the results obtained for the $R = 2$ a.u. equilibrium internuclear distance of H_2^+ are summarized. Fig. 3.9 shows the obtained ionization probability densities as a function of electron momentum component perpendicular (k_x) and parallel (k_z) to the laser field's polarization vector for the $E_0 \in \{0.25, 0.5, 0.75, 1\}$ a.u. electric field amplitudes.

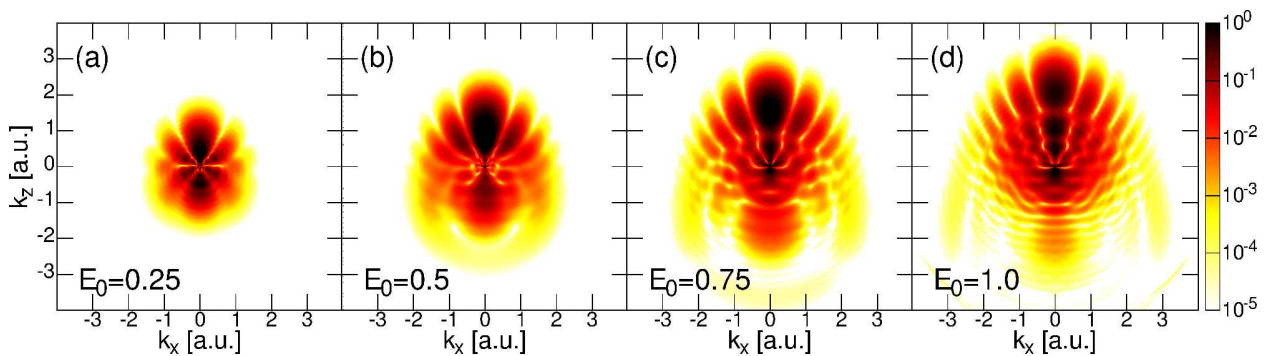


Figure 3.9: Laser induced photoelectron spectra as a function of electric field amplitude [(a) $E_0 = 0.25$ a.u., (b) $E_0 = 0.5$ a.u., (c) $E_0 = 0.75$ a.u., (d) $E_0 = 1$ a.u.] calculated for the $R = 2$ a.u. equilibrium internuclear distance after the completion of the external field ($t = \tau$). On the x-axis electron momentum component perpendicular (k_x), on the y-axis parallel (k_z) to the laser polarization vector is shown.

At first sight two straightforward observations could be made. According to the first one - which is an obvious and expected behavior - with the increase of the field's intensity the ionization probability of the electrons is distributed along a larger region of the momentum space (more intense radiations causes larger measurable maximum electron energies). While, for the lowest $E_0 = 0.25$ a.u. field the maximum of the ionization probability densities is situated around the value of $k_z = 0.5$ a.u. (meaning a $\mathcal{E}_{\text{kin}} = (k_x + k_z)^2/2 = 0.125$ a.u. electron energy) the maximum is shifted to the high momentum value of $k_z = 2$ a.u. for the case of the extremely high intensity ($E_0 = 1$ a.u.), corresponding to $\mathcal{E}_{\text{kin}} = 2$ a.u. electron energy. The scaling of the largest probability of photoelectron energies with the amplitude of the electric field can be given by the expression $\mathcal{E}_{\text{kin,max}}^{(2)}/\mathcal{E}_{\text{kin,max}}^{(1)} = (E_0^{(2)}/E_0^{(1)})^2$, which for the discussed cases gives a factor of 16 magnification in maximum electron energy by increasing the amplitude from $E_0 = 0.25$ a.u. to $E_0 = 1$ a.u.. The linear scaling between k_{max} and E_0 was obvious only by looking at the plots calculated for the four different laser field intensities.

The second observation was, that the PES images become more and more complicated by increasing the external field's strength. As it can be observed, in the case of the lowest electric field amplitude very few features appeared in the spectra, while for the largest E_0

amplitude the pattern became quite complex and hard to be deciphered. This increase in the complexity of the PES images can be explained by the fact, that as the intensity of the radiation is increased the dynamics of the continuum EWPs became more diversified.

In addition to that, well structured minimum radial patterns appeared in all cases, which are basically *interference minima of the signal and reference EWPs*. The location of these minima were proven to be dependent on the z_0 maximum distance that the signal electron reached before the return to its parent ion, a parameter that can be directly controlled by the intensity of the laser field: by increasing E_0 the value of z_0 also increases.

Beside these two first-sight observations, it was also observed, that by increasing E_0 the number of radial interference minima appearing in the forward ejection region ($k_z > 0$) increased. By considering only the positive momentum component part of the forward ejection region ($k_x > 0, k_z > 0$) in the case of $E_0 = 0.25$ a.u. two minima were detected, while by increasing the field amplitude the number of minima increased to 3 ($E_0 = 0.5$ a.u.), 4 ($E_0 = 0.75$ a.u.) and 5 ($E_0 = 0.75$ a.u.). The number of appearing interference minima is again the direct consequence of the strength of the radiation field, which as it gets more and more increased drives the signal EWP to larger and larger z_0 distances.

Another interesting feature that appeared in the PES when E_0 was increased to 0.75 a.u. and above that, to 1 a.u., was that in the low momentum part of the spectra a second interference pattern occurred. For $E_0 = 0.75$ a.u. these secondary structures are located at $k_z < 1$, while for $E_0 = 1$ a.u. they appear below the parallel momentum component value $k_z < 1.5$ a.u.. These two distinct interference pattern regions - obtained for the high intensity fields - are the direct consequence of two distinct interference mechanisms. While in the case of lower field strengths (i.e., $E_0 \in \{0.25, 0.5\}$) only the primary dominant mechanism is observable - interference between EWPs created during the same optical half-cycle -, for higher electric field strengths a secondary mechanism become detectable, which can be attributed to an additional ejection of EWPs: the ejection of a secondary pair of reference and signal EWPs occurring at a different part, at another half-cycle, of the pulse.

This secondary feature, that modified the low momentum part of the primary interference pattern (last two subfigures of Fig. 3.9), is attributed to the different values of the vector potential $\vec{A}(t)$ in these two distinct optical half-cycles, i.e., in the instances when these two pairs of EWPs were ejected into the continuum by the radiation field.

3.5 The effect of the molecular potential on the photoelectron hologram

The main goal of this thesis was to investigate the structure of the photoelectron holograms for molecular targets, i.e., how the geometry of the molecule is influencing the hologram. To this end the PES obtained for the H_2^+ target with different internuclear separations interacting with a few cycle laser pulse with the following parameters (laser frequency $\omega = 0.4445$ a.u., pulse duration $\tau = 28.26$ a.u., and the electric field amplitude $E_0 = 0.5$ a.u.) is presented. Based on previous [26, 27, 29, 30] studies it is well known that the shape of the hologram is predominantly influenced by two factors. The first one is the spatial path of the strongly scattered (signal) electron trajectory [26, 29, 30], which is characterized by the z_0 parameter meaning the maximum distance reached by the continuum EWP before the rescattering event. The second factor is the potential experienced in the immediate vicinity of the target by the returning electron along the signal trajectory [27].

In order to identify the influence of the molecular binding potential on the photoelectron hologram, calculations for a model system with a spherically symmetrical potential - having the same asymptotic form as the H_2^+ target - were also performed, which during the interaction with a few cycle laser field it produces the similar signal electron trajectory as the H_2^+ target (i.e., it has the same z_0 parameter). This second condition can be fulfilled by ensuring that the I_p ionization energy of the model potential and the H_2^+ target is the same. If these two conditions are met, than the differences observed in the PESs can be directly attributed to the difference between the binding potentials in the immediate vicinity of the targets [27]. This model potential was constructed by performing the molecular axis orientation averaging of the potential created by the two nuclei of the H_2^+ , which leads to the following form

$$V_{\text{mod}}(r) = \begin{cases} -2/r & , \text{ if } r \geq R/2; \\ -4/R & , \text{ if } r < R/2, \end{cases} \quad (3.3)$$

where R is the internuclear distance of the H_2^+ target. Compared to H_2^+ , the ionization energy of the model system became lower (since the deep potential well around the cores disappeared as a result of the orientation averaging), thus, in order to ensure the same ionization energy the model potential should have been modified by performing the following substitution $R \rightarrow R_{\text{equiv}}$, where R_{equiv} is a model parameter. The value of R_{equiv} for each internuclear separation is listed in Table 3.1.

Table 3.1: The values of the equivalent internuclear distances used for the model target system.

R [a.u.]	R_{equiv} [a.u.]
1.0	0.92
2.0	1.72
4.0	3.01

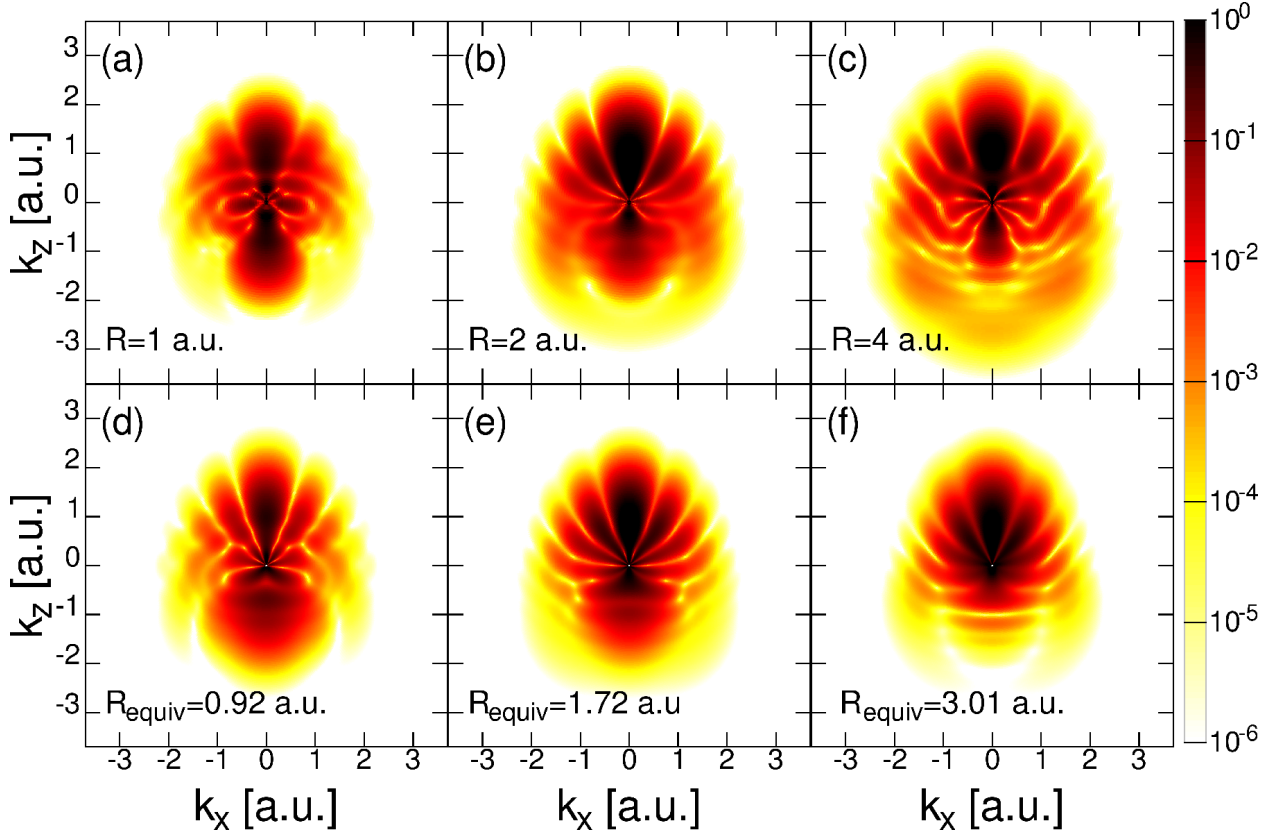


Figure 3.10: The converged photoelectron spectra calculated for the H_2^+ (first row) are shown for different internuclear distances: (a) $R = 1$ a.u., (b) $R = 2$ a.u., (c) $R = 4$ a.u.. The $\text{H}_{2\text{mod}}^+$ results corresponding to each internuclear separation are shown below the H_2^+ . For a given R the ionization energy of the H_2^+ and $\text{H}_{2\text{mod}}^+$ targets is the same: $I_p^{(a)} = I_p^{(d)}$; $I_p^{(b)} = I_p^{(e)}$; $I_p^{(c)} = I_p^{(f)}$.

By comparing the PES obtained for the H_2^+ (first row of Fig. 3.10) target and for its model system ($\text{H}_{2\text{mod}}^+$, second row of Fig. 3.10), at first sight similarities could be observed between the spectra calculated for the corresponding R - R_{equiv} pairs [Fig. 3.10(a) \Leftrightarrow (d); (b) \Leftrightarrow (e); (c) \Leftrightarrow (f)]. These similarities between the holograms obtained for the molecule and for its corresponding model is not surprising, since the model system was constructed in such a way that the IPs of both system were identical. Thus, under the action of the same driving field the direct and scattered paths were roughly the same for both targets, which ensured that the phases accumulated by the electron along these paths were similar for both systems.

Therefore, the differences can be directly attributed to the fact that in the neighborhood of the targets the binding potentials differ. This difference was illustrated in Fig. 3.11, where $\rho[V(\rho, z) - V_{\text{mod}}(\rho, z)]$ is shown in the $\rho O z$ plain (with $\rho = \sqrt{x^2 + y^2}$ denoting the cylindrical coordinate).

The discrepancies between the holograms obtained for H_2^+ and for its model were further investigated by comparing (Fig. 3.12) the angular distribution of photoelectrons at a fixed electron momentum value ($k = 1.5$ a.u.) for different internuclear separations. For each internuclear distance in the forward electron ejection direction ($\theta_k \leq 90^\circ$) the deep minima associated with the spatial interference can be clearly identified for both systems. Moreover,

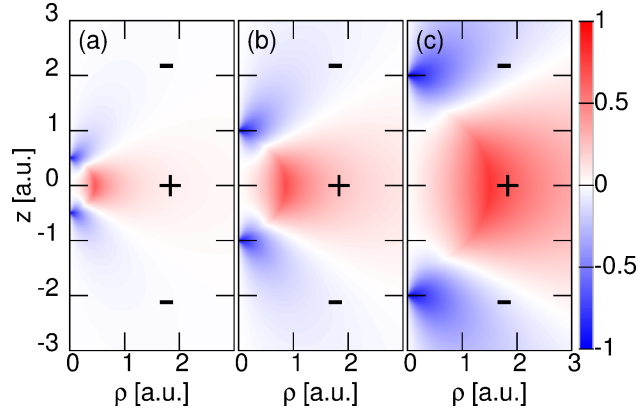


Figure 3.11: The value of $\rho[V(\rho, z) - V_{\text{mod}}(\rho, z)]$, where ρ and z are the cylindrical coordinates, calculated for the corresponding pairs: (a) $R(\text{H}_2^+) = 1$ a.u., $R_{\text{equiv}}(\text{H}_{2\text{mod}}^+) = 0.92$ a.u.; (b) $R(\text{H}_2^+) = 2$ a.u., $R_{\text{equiv}}(\text{H}_{2\text{mod}}^+) = 1.72$ a.u.; (c) $R(\text{H}_2^+) = 4$ a.u., $R_{\text{equiv}}(\text{H}_{2\text{mod}}^+) = 3.01$ a.u..

the electron ejection angles at which these interference minima appeared roughly coincides for both targets. However, in the case of the model system, regardless of the internuclear distance, the interference minima were found to be systematically located at slightly smaller electron ejection angles, which translates to a slightly denser (smaller angular separation between the interference minima) hologram for the model target.

The denser hologram in the case of the model target can be directly attributed to the fact that the returning electron along a large portion of scattered trajectory meets a deeper binding potential [27]. This is confirmed in Fig. 3.11, where it can be observed, that with the notable exception of the immediate vicinity of the H_2^+ cores $\rho[V(\rho, z) - V_{\text{mod}}(\rho, z)] \geq 0$.

Based on the above arguments, it is clear, that the observed differences between the holograms of the real H_2^+ target and its model can be attributed to the difference between the two-center binding potential of H_2^+ and the central binding potential of the model target. Nonetheless, in the hologram of the H_2^+ target obvious traces of the two-center interference [54,55] were not observed at first sight. This can be explained by the fact that the two dominant continuum EWPs were created during an optical half-cycle [26,27] of the driving field, and during a relatively large (compared to the laser field period) duration of time. Each of these two dominant continuum EWPs can be decomposed into smaller continuum wave packets, which are created over a short period of time in which the vector potential can be considered constant. In these smaller continuum EWPs the two-center interference pattern might be present, however after the completion of the laser pulse, when these wave packets are coherently added, the interference pattern is most probably averaged out since each of the smaller wave packets is shifted in momentum space in accordance with the vector potential of the laser field in their creation moment.

Traces of the two-center interference appear to be present as a modulation in the depth of the spatial interference minima. Fig. 3.13 shows the depth of the spatial interference minimum, observable around the $\theta_k = \pi/8$ electron ejection angle in Fig. 3.10(b), as a function of the electron ejection momentum for the H_2^+ target and for its model as well. The high momentum ($k > 1.5$ a.u.) minimum observable only in the H_2^+ curve is located closely

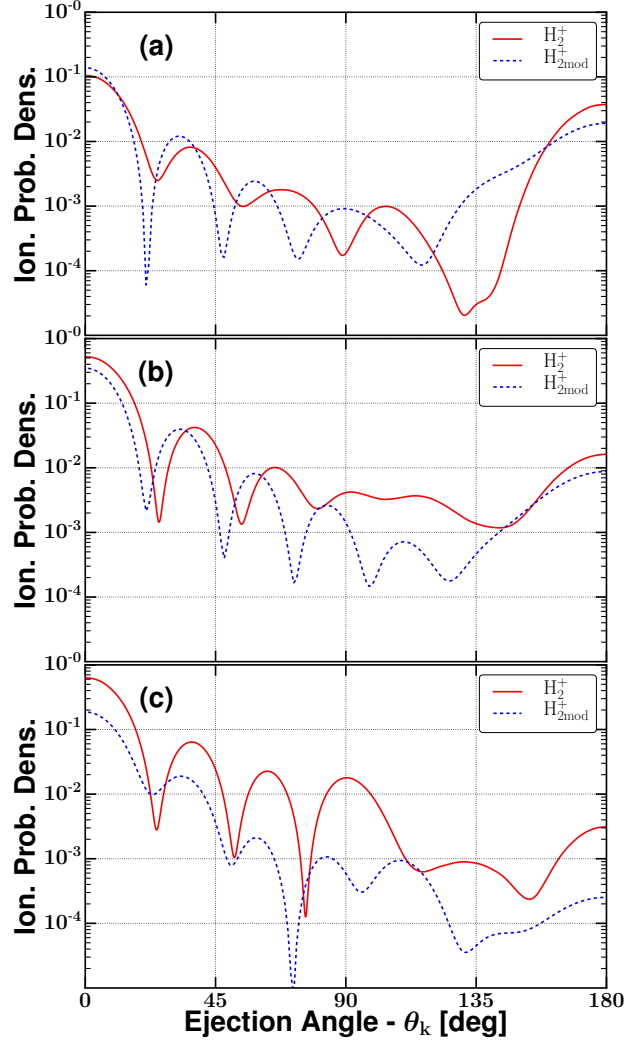


Figure 3.12: The angular distribution of photoelectrons at the fixed $k = 1.5$ a.u. momentum value for the different targets: (a) $R(\text{H}_2^+) = 1$ a.u., $R_{\text{equiv}}(\text{H}_{2\text{mod}}^+) = 0.92$ a.u.; (b) $R(\text{H}_2^+) = 2$ a.u., $R_{\text{equiv}}(\text{H}_{2\text{mod}}^+) = 1.72$ a.u.; (c) $R(\text{H}_2^+) = 4$ a.u., $R_{\text{equiv}}(\text{H}_{2\text{mod}}^+) = 3.01$ a.u..

to the two-center interference minimum predicted by the simple model of Nagy *et al.* [56], where the two-center interference pattern was shown to be proportional to $\sim \cos^2\left(\frac{\vec{k}\cdot\vec{R}}{2}\right)$. The shift in the location of the H_2^+ minimum appears due to the nonzero vector potential in the time moment when the continuum EWP showing the deep minimum was created. The minima observable for both the H_2^+ and its model at low electron momentum values are the result of the interference between the EWPs created during the second and third half cycle of the laser field [27].

The internuclear distance dependence of the photoelectron hologram was shown on Fig. 3.10, where it can be observed that by increasing the internuclear distance from 1 a.u. to 4 a.u. the density of the hologram has also increased. This behavior of the hologram can be clearly observed on Fig. 3.14, where the angular distribution of photoelectrons emitted with asymptotic momentum $k = 2$ a.u. were shown for different R values. The number of spatial interference minima in the forward electron ejection region ($\theta_k < 90^\circ$) for the $R=1$ a.u. internuclear distance is 3, which increased to 4 for the $R = 2$ a.u. and $R = 4$ a.u. internuclear

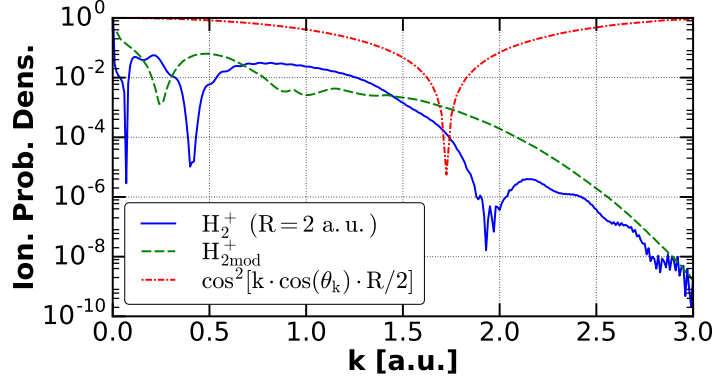


Figure 3.13: PES values along the first spatial interference minimum calculated for H_2^+ and for the $H_{2\text{mod}}^+$ model plotted next to $\cos^2(\vec{k} \cdot \vec{R}/2) \equiv \cos^2[k \cdot \cos(\theta_k) \cdot R/2]$.

distances. Moreover, the 4th interference minimum for $R = 4$ a.u. is located at smaller electron ejection angle than the 4th interference minimum for $R = 2$ a.u. Consequently, the average angular separation between the interference minima decreases (i.e., the density of the interference pattern increases) as the internuclear distance gets larger.

This increase in the interference pattern's density with increasing internuclear separation is indirectly induced by the drop-off of the ionization energy with the increase of R . For a fixed driving laser pulse the decrease in the IP leads to the increase of the initial velocity of the created continuum EWP, which in turn leads to longer electron trajectories prior to the rescattering event. With the increase of the electron trajectory length (i.e., with the increase of the z_0 parameter) the density of photoelectron hologram also increased.

Despite the considerable change of the H_2^+ ionization energy from 1.451 a.u. to 0.796 a.u. when the internuclear distance is increased from 1 to 4 a.u., a drastic change in the interference pattern's density was not observed. This can be explained by considering that the expected increase of the interference pattern's density was tempered due to the fact, that with increasing R the depth of the binding potential experienced by the returning electron decreased, which in turn lowered the density of the hologram.

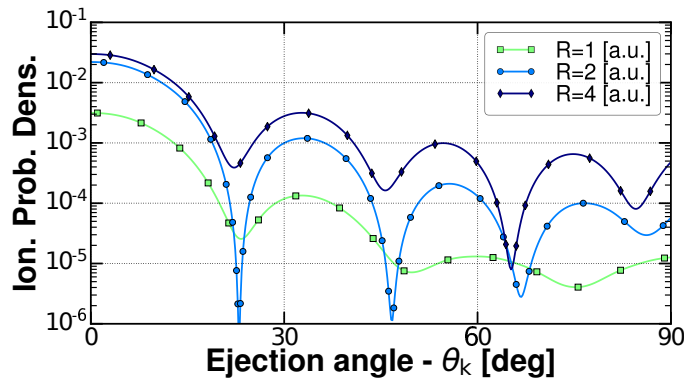


Figure 3.14: The $k = 2$ a.u. segments of the photoelectron spectra zoomed to the ejection region $\theta_k < 90^\circ$ calculated for the H_2^+ molecule for the different R internuclear separations.

4. Conclusions

In the first part of the thesis I have presented two different theoretical approaches that were implemented to investigate laser induced electron dynamics in small atomic systems. The first approach was a semi-classical method based on the *strong-field approximation* (SFA) scheme, where the simple three-step model of SFA was used and the acceleration of the tunnel-ionized electron calculated in the presence of the oscillating field. In the recombination process of the ionized electron to the parent ion - which mechanism is responsible for the creation of the *high harmonic generation* (HHG) pulses - also the Stark-shift of the ground state of the hydrogen atom in the presence of the oscillatory electric field was included, and the characteristics of the HHG spectra investigated as a function of laser parameters. With the implemented method the expected increase of the HHG plateau was obtained, where the last (highest energy photon) harmonic in the plateau region is resulted from the reabsorption of a high energy electron that releases its $3.17U_p + I_p$ exes energy gained from the radiation field. The U_p ponderomotive energy increased with increasing the wavelength and/or the electric field amplitude of the laser pulse ($U_p \sim \lambda^2 E_0^2$). The obtained behavior of the HHG spectra may give us further possibilities to introduce the (CPU parallelized) calculations into more complex numerical codes, where the macroscopic effects of the laser propagation through medium are investigated.

Beside this semi-classical approach - that was used to calculate the dynamics of the reabsorbed laser driven electrons - two other methods were discussed as well, which were based on the solution of the *time-dependent Schrödinger equation* (TDSE), and which can be used to extract a full physical picture regarding the behavior of ejected electronic wave packets. For the solution of the TDSE two different approaches were considered and numerically implemented: the *iterative solution* (iTSE model) and the *direct solution* (TDSE method) of the *momentum space TDSE*, which were employed to calculate and compare the laser induced photoelectron spectra obtained for the hydrogen atom.

In the principle part of the present thesis the photoelectron holography of a diatomic molecule considered with a *single active electron* (SAE) was studied. This goal was achieved by implementing first a numerical method which is based on the direct solution of the TDSE for the XUV laser field irradiated system. As target the H_2^+ molecule was considered and the interaction with a few-cycle (ultrashort) XUV laser pulse was studied. The electronic wave function and the Hamiltonian of the system was represented in the *prolate spheroidal coordinate* system and on a *finite-element discrete variable representation* (FE-DVR) grid, where in each finite element the wave function was expanded in the basis of local Lagrange interpolating polynomials. As the first step the accuracy of the grid representation was checked, and accurate/convergent bound state (BS) energies and wave functions of H_2^+ were obtained by the direct diagonalization of the field-free Hamiltonian. With the calculated

BSs accurate *potential energy curve* and *electronic transition dipole moments* were obtained, which can be included in further calculations where the nuclear dynamics are also involved in the laser induced processes. Another important element in the study of the laser induced EWP dynamics was the calculation of the initial (ground) state wave function of the target, which was later on propagated in time by using the short-iterative Lanczos algorithm. In this time propagation scheme a *complex absorbing potential* (CAP) was also built in to eliminate the reflections from the edge of the simulation box, and to control the size of the grid (i.e., if absorption is detected at the CAP, then the size of the simulation box was extended) in order to reduce as much as possible the absorptions at the boundary (to reduce the information losses at the end of the simulation box). With the implementation of the time-propagation algorithm the electron dynamics was investigated: first, the *occupation probabilities* of different bound states as a function of time for different field intensities. The major dynamics and their temporal location were identified, and it was also shown that a not negligible contribution from different bound states still remained in the *time-dependent wave function* (TDWF) after the conclusion of the external field. These remnant small contributions were removed from the wave function prior to calculating the *photoelectron spectra* (PES) in order to reduce the possible error that the projection of the TDWF onto the approximate one-center continuum states would bring into the image of the spectra. Using the presented theoretical tool the dependence of the photoelectron spectra as a function of molecular internuclear distance was studied.

The accurate PES and *photoelectron holograms* (i.e., interference patterns created in the PES by the interference between the scattered and reference electronic wave packets) were obtained after performing rigorous convergence tests, implying the convergence as a function of number of the subtracted bound states and as a function of propagation time after the completion of the laser field. In order to identify how the spatial profile of the molecular binding potential influences the shape of the photoelectron spectra obtained for the H_2^+ also a one-center model system ($\text{H}_{2\text{mod}}^+$) with the same ionization energy and long range potential as H_2^+ was considered. Provided that the same XUV pulses were used and the aforementioned conditions were satisfied when constructing the potential of the model system, similar scattered and reference *electronic wave packet* (EWP) trajectories were produced for both targets. As expected, roughly similar PESs were obtained for both systems, and it was shown that the differences between the calculated patterns are the direct consequence of the differences in the parent ion's binding potential that the rescattering (signal) electron meets along the returning path: higher density locations of minima were obtained if the potential along the signal path was deeper.

Furthermore, it was shown that the locations of the PES minima obtained for the H_2^+ molecule changed as the internuclear separation R was modified. As the internuclear separation R was increased a denser interference pattern was observed, which is the result of the interplay between two opposite factors. First, by increasing R the ionization energy of the target molecule became lower, which implicitly means that the ionized electron had a higher

initial velocity. As a consequence, this electron departed at a larger distance measured from the parent ion, meaning a higher z_0 parameter before the returning event. If the value of z_0 is increased a higher density in the hologram appears. However, the second factor weakened this effect, since for higher R internuclear distances the signal electron met a shallower binding potential, hence the density of the hologram was decreased. As a future perspective, further investigations may be carried out in order to identify and to quantify the effects of these two distinct processes that are responsible for the shift of the minima location in the PES, which opens the possibility of extracting information from the holographic image regarding for example the value of internuclear distance in the instance, when the signal and direct EWPs were emitted into the continuum.

According to the calculated EWP dynamics it was shown that the dominant EWPs, which are responsible for the creation of the well identifiable interference minima appearing in the PES, were “born” in the second and third optical half-cycle of the oscillating field, while obvious presence of the *two-center interference* effects (expected as horizontal interference patterns parallel to the k_x axis) were not detectable in the holographic image. This could be explained by the fact that these EWPs can be decomposed into smaller EWPs which on the other hand are shifted in the momentum space in accordance with the value of the external field’s vector potential in their creation moment, and when these smaller EWPs are coherently added the two-center interference pattern is most probably averaged out. However, by carefully analyzing the PES of the H_2^+ molecule along the first minimum, traces of the two-center interference appeared to be present as a modulation in the depth of the spatial interference minimum (near the location where it was predicted by simple models).

In the final part of this work also the features of the holograms were investigated as a function of field intensity, and it was found that for high external electric field strengths more interference minima appeared in the PESs (higher interference pattern density) and more complex patterns were obtained. The higher complexity of the holographic patterns obtained for the higher intensity fields was due to the fact that a secondary EWP interference mechanism appeared in the lower momentum part of the photoelectron spectra.

The developed method opens further possibilities to calculate PESs for numerous internuclear separations (provided that a sufficiently large CPU time is available) and to identify the density of the interference patterns as a function of R , while also other investigations may be carried out by using different ultrashort laser pulses, where the inclusion of the nuclear dynamics may be a possible next goal.

List of publications

- ISI articles indexed in Web of Science (Knowledge) database:

- G.Zs. Kiss, S. Borbély, A. Tóth, and L. Nagy, *Photoelectron holography of the H_2^+ molecule* [sent for publication] .
- G.Zs. Kiss, S. Borbély, and L. Nagy, *Efficient numerical method for investigating diatomic molecules with single active electron subjected to intense and ultrashort laser fields* AIP Conf. Proc. **1916**, 020010 (2017).
- A. Tóth, S. Borbély, G.Zs. Kiss, G.J. Halász, and Á. Vibók, *Towards the Full Quantum Dynamical Description of PhotonInduced Processes in D_2^+* J. Phys. Chem. A **120**, 9411 (2016).
- G.Zs. Kiss, S. Borbély, and L. Nagy, *An efficient numerical discretization method for the study of the H_2^+ in intense laser fields*, AIP Conf. Proc. **1694**, 200171 (2015).
- G.Zs. Kiss, S. Borbély, and L. Nagy, *Momentum Space Iterative Solution of the Time-Dependent Schrödinger Equation*, AIP Conf. Proc. **1564**, 78 (2013).
- S. Borbély, G.Zs. Kiss, and L. Nagy, *The Excitation and Ionization of the Hydrogen Atom In Strong Laser Fields*, Central European Journal of Physics **8**, 249 (2010).

- other (non-ISI article) publication:

- Kiss Gellért Zsolt et al., (in Hungarian) "*Numerikus módszerek intenzív lézertér és atomok közötti kölcsönhatás elméleti tanulmányozására*", Conf. proc.: "A fizika, matematika és művészet találkozása az oktatásban, kutatásban" / ISBN 978-963-284-346-9, pp.207-212, ELTE TTK (2013) ,

Oral presentations at international conferences

G.Zs. Kiss, S. Borbély, and L. Nagy, *Photon Induced Electron Dynamics in Diatomic Molecules by XUV Laser Pulses*, Joint ISCP-INDLAS Conference organized by National Institute for Laser Plasma & Radiation Physics (INFLPR), 03-07 September 2018, Alba-Iulia, Romania

G.Zs. Kiss, S. Borbély, and L. Nagy, *Efficient Numerical Method for Investigating Diatomic Molecules in Intense and Ultrashort laser Fields*, TIM17 Physics Conference, organized by the West University of Timișoara, 25-27 May 2017, Timișoara, Romania

G.Zs. Kiss, S. Borbély, and L. Nagy, *The Numerical Solution of The Time-Dependent Schrödinger Equation for Atoms in Intense Laser Fields*, PHYSICS CONFERENCE TIM-12 organized by the West University of Timișoara, 27-30 November 2012, Timișoara, Romania

Poster presentations at international conferences

- "Laser-atom interaction beyond the strong field approximation model" [Processes in Isotops and Molecules (PIM) 11th International Conf., Cluj, RO, 27-29/09/2017]
- "Efficient numerical method for investigating diatomic molecules with single active electron subjected to intense and ultrashort XUV laser fields." [14th International Conference on Multiphoton Processes, Budapest, HU, 24-27/09/2017]
- "Theoretical Investigation Beyond the Strong Field Approximation Model" [TIM17 Physics Conference, Timișoara, Romania, 25-27/05/2017]
- "Theoretical Study of the Dihydrogen Cation Irradiated with Intense XUV Laser Fields" [TIM17 Physics Conference]
- "Numerical Method to Investigate Diatomic Molecules with Single Active Electron Subjected to Intense Laser Fields" [4th XLIC General Meeting, Prague, Czechia, 14-16/03/2017]
- "Numerical investigations beyond the SFA model." (G.Zs. Kiss, K.Kovács, V. Toa) [MEDEA: Ultrafast Dynamics with Intense Radiation Sources, Crete, Greece, 18-22/10/2016]
- "Investigation of the Electronic Wave Packet Dynamics of the H_2^+ Molecule Subjected to External Laser Field" [XUV/X-ray light and fast ions for ultrashort chemistry (XLIC) 3rd General Meeting, Debrecen, HU, 2-4/09/2015]
- "Investigation of the H_2^+ molecule by strong, ultrashort laser pulses" [Workshop 2015: "Photon and fast Ion induced Processes in Atoms, Molecules and Nanostructures" (PIPAMON), Debrecen, 24-26/03/2015]
- "Photionization of Atoms and Molecules (H_2^+) Irradiated with Ultrashort and Strong Laser Pulses" (G.Zs.Kiss et al.) [Work shop: Autumn School on Laser Dynamics, Bolyai Institute, University of Szeged, 24-28/09/2014, Szeged, HU]
- "Ionization of The H_2^+ Molecule by Ultrashort EUV/XUV Laser Pulses" (G.Zs.Kiss, et al) [COST CM1204 Madrid, 11-13/09/2013]
- "Numerical Method for The Investigation of H_2^+ Molecule In External XUV Laser Field" ["PHYSICS CONFERENCE TIM-14" organised by the West University of Timișoara, 27-30/09/2012, RO]
- Solving the TDSE by Using Levin's Integration Method (G.Zs. Kiss, S.Borbély, L.Nagy) [4th anual meeting of the COST Action CUSPFEL, 21-23/03/2012, Cluj, Romania]

Poster contributions

- "Dissociative ionization of D_2^+ in strong laser fields." (A. Tóth, S. Borbély, G.Zs. Kiss, G. Halász, and Á. Vibók) [MEDEA: Ultrafast Dynamics with Intense Radiation Sources, Crete, Greece, 18-22/10/2016]
- Iterative Solution of The Time-Dependent Schrödinger Equation (S. Borbély, G.Zs. Kiss, L.Nagy) [44th CONF. ON THE EUROPEAN GROUP ON ATOMIC SYSTEMS, 9-13/07/2012, Göthenburg]

List of abbreviations

ATI	above-threshold ionization
BS	bound state
CAP	complex absorbing potential
CEP	carrier-envelope phase
CN	Crank-Nicolson method
CPA	chirped pulse amplification
CPU	central processing unit (i.e., computer processor)
CTMC	classical trajectory Monte-Carlo method
EWP	electron wave packet
FD	finite difference method
FE-DVR	finite-element discrete variable representation
WF	wave function
HHG	high harmonic generation
HM	holographic mapping
IP (or I_p)	ionization potential
iTDSE	iterative time-dependent Schrödinger equation method
LASER	light amplification by stimulated emission of radiation
LIED	light induced electron diffraction
MPI	multi-photon ionization
MSSFA	momentum-space strong field approximation
OBI	over-the-barrier ionization
ODE	ordinary differential equation
OpenMPI	Open Message Passing Interface
OP	occupation probability
PEC	potential energy curve
PEH	photoelectron hologram
PES	photoelectron spectrum
PSC	prolate spheroidal coordinates
SAE	single active electron approximation
SFA	strong field approximation
SI	single photon ionization
SLEPc	Scalable Library for Eigenvalue Problem Computations
TDCC	time-dependent close coupling methods
TDSE	time-dependent Schrödinger equation
TDWF	time-dependent wave function
TI	tunnelling ionization
XUV	extreme ultraviolet

Bibliography (selected References)

- [1] A. L. Schawlow and C. H. Townes. Infrared and optical masers. *Phys. Rev.*, 112:1940–1949, Dec 1958.
- [2] A. Einstein. The quantum theory of radiation. *Physikalische Zeitschrift*, 18:121, 1917.
- [3] T. Maiman. Stimulated optical radiation in ruby. *Nature (London)*, 187:493, 1960.
- [4] B. Baier, A. Kern, L. Kaderali, B. Bis, D. Koschel, and A. Rolle. Retrospective survival analysis of 237 consecutive patients with multiple pulmonary metastases from advanced renal cell carcinoma exclusively resected by a 1318-nm laser. *Interact Cardiovasc Thorac Surg.*, 21:211–217, 2015.
- [5] D.S. Fink, H. Sibley, M. Kunduk, and et al. Subjective and objective voice outcomes after transoral laser microsurgery for early glottic cancer. *Laryngoscope*, 126:405–407, 2016.
- [6] T. Sakimoto, M.I. Rosenblatt, and D.T. Azar. Laser eye surgery for refractive errors. *The Lancet*, 367:1432–1447, 2006.
- [7] D. Ortega-Concepcin, J.A. Cano-Durn, J.-F. Pea-Cardelles, V.-M. Paredes-Rodriguez, J. Gonzalez-Serrano, and J. Lpez-Quiles. The application of diode laser in the treatment of oral soft tissues lesions. a literature review. *J Clin Exp Dent.*, 9:925–928, 2017.
- [8] B.M. Toregard. Laser applications in cosmetic surgery. *Ann Chir Gynaecol*, 79:208, 1990.
- [9] A.H. Zewail. Femtochemistry: atomic-scale dynamics of the chemical bond. *J. Phys. Chem*, 104:5660–5694, 2000.
- [10] W. Yu, M.Y. Yu, H. Xu, and Y.W. Tian. Intense local plasma heating by stopping of ultrashort ultraintense laser pulse in dense plasma. *Laser and Particle Beams*, 25:661–638, 2007.
- [11] K. Ikeda et al. Selective crystallization of the metastable phase of indomethacin at the interface of liquid/air bubble induced by femtosecond laser irradiation. *Applied Physics Express*, 8:045501, 2015.
- [12] V. Lazar. World premiere: The laser in magurele has reached peak power 10 petawatts, 13.03.2019.
- [13] G.A. Mourou and V. Yanovsky. Relativistic optics: A gateway to attosecond physics. *Optics and Photonics News*, 15:40–45, 2004.
- [14] F. Krausz and M. Ivanov. Attosecond physics. *Rev. Mod. Phys.*, 81, 2009.
- [15] A. Einstein. Über einen die erzeugung und verwandlung des liches betreffenden heuristischen gesichtspunkt. *Annalen der Physik*, 17:132–148, 1905.
- [16] M. Planck. Über eine verbesserung der wien’schen spectralgleichung. *Verhandlungen der Deutschen Physikalischen Gesellschaft*, 2:202–204, 1900.
- [17] P.B. Corkum. Plasma perspective on strong field multiphoton ionization. *Physical Review Letters*, 71:1994, 1993.
- [18] A. L’Huillier, Ph. Balcou, S. Candel, K.J. Schafer, and K.C. Kulander. Calculations of high-order harmonic-generation processes in xenon at 1064 nm. *Phys. Rev. A*, 46:2778–2790, Sep 1992.
- [19] M. Peters, T.-T. Nguyen-Dang, E. Charron, A. Keller, and O. Atabek. Laser-induced electron diffraction: A tool for molecular orbital imaging. *Phys. Rev. A*, 85, 2012.
- [20] T. Marchenko, Y. Huismans, K. J. Schafer, and M. J. J. Vrakking. Criteria for the observation of strong-field photoelectron holography. *Phys. Rev. A*, 84:053427, Nov 2011.

Bibliography (selected References)

- [21] X.-B. Bian, Y. Huismans, O. Smirnova, K.-J. Yuan, M.J.J. Vrakking, and A.D. Bandrauk. Subcycle interference dynamics of time-resolved photoelectron holography with midinfrared laser pulses. *Phys. Rev. A*, 84:043420, Oct 2011.
- [22] G. Porat, G. Alon, S. Rozen, O. Pedatzur, M. Krüger, D. Azoury, A. Natan, G. Orenstein, B. D. Bruner, M.J.J. Vrakking, and N. Dudovich. Attosecond time-resolved photoelectron holography. *Nature Communications*, 9, 2018.
- [23] D.G. Arbó, E. Persson, and J. Burgdörfer. Time double-slit interferences in strong-field tunneling ionization. *Phys. Rev. A*, 74:063407, Dec 2006.
- [24] Y. Huismans, A. Gijsbertsen, A.S. Smolkowska, J.H. Jungmann, A. Rouzée, P.S.W.M. Logman, F. Lépine, C. Cauchy, S. Zamith, T. Marchenko, J.M. Bakker, G. Berden, B. Redlich, A.F.G. van der Meer, M. Yu. Ivanov, T.-M. Yan, D. Bauer, O. Smirnova, and M.J.J. Vrakking. Scaling laws for photoelectron holography in the midinfrared wavelength regime. *Phys. Rev. Lett.*, 109:013002, Jul 2012.
- [25] D.D. Hickstein, P. Ranitovic, S. Witte, X.-M. Tong, Y. Huismans, P. Arpin, X. Zhou, K.E. Keister, C.W. Hogle, B. Zhang, C. Ding, P. Johnsson, N. Tushima, M.J.J. Vrakking, M.M. Murnane, and H.C. Kapteyn. Direct visualization of laser-driven electron multiple scattering and tunneling distance in strong-field ionization. *Phys. Rev. Lett.*, 109:073004, Aug 2012.
- [26] S. Borbély, A. Tóth, K. Tókési, and L. Nagy. Spatial and temporal interference during the ionization of h by few-cycle xuv laser pulses. *Phys. Rev. A*, 87:013405, Jan 2013.
- [27] S. Borbély, A. Tóth, D. G. Arbó, K. Tókési, and L. Nagy. Photoelectron holography of atomic targets. *Phys. Rev. A*, 99:013413, Jan 2019.
- [28] S. López and D. Arbo. Holographic interferences in photoelectron spectra: different approaches. *The European Physical Journal D*, 73:28, Feb 2019.
- [29] S. Borbély, A. Tóth, K. Tókési, and L. Nagy. Laser-induced electron diffraction in a pumpprobe setup using half-cycle electric pulses. *Physica Scripta*, 2013(T156):014066, 2013.
- [30] A. Tóth, S. Borbély, K. Tókési, and L. Nagy. Ionization of atoms by few-cycle euv laser pulses: carrier-envelope phase dependence of the intra-pulse interference effects. *The European Physical Journal D*, 68(11):339, 2014.
- [31] X.-B. Bian and A.D. Bandrauk. Attosecond time-resolved imaging of molecular structure by photoelectron holography. *Phys. Rev. Lett.*, 108:263003, Jun 2012.
- [32] M. Meckel, A. Staudte, S. Patchkovskii, D. M. Villeneuve, P. B. Corkum, R. Doerner, and M. Spanner. *NATURE PHYSICS*, 10(8):594–600, 2014.
- [33] X.-B. Bian and A.D. Bandrauk. Orientation-dependent forward-backward photoelectron holography from asymmetric molecules. *Phys. Rev. A*, 89:033423, Mar 2014.
- [34] H. Marko, X.-B. Bian, M. Spanner, A. Staudte, and P.B. Corkum. Probing molecular dynamics by laser-induced backscattering holography. *Phys. Rev. Lett.*, 116:133001, Apr 2016.
- [35] Y. Li, Y. Zhou, M. He, M. Li, P. Lan, and P. Lu. Time-resolved internal-electron-scattering effect of H_2^+ in enhanced ionization regions. *Phys. Rev. A*, 94:013422, Jul 2016.
- [36] M. He, Y. Zhou, Y. Li, M. Li, and P. Lu. Revealing the target structure information encoded in strong-field photoelectron hologram. *Optical and Quantum Electronics*, 49(6):232, May 2017.
- [37] H. Miyagi, T. Morishita, and S. Watanabe. Electron scattering and photoionization of one-electron diatomic molecules. *Phys. Rev. A*, 85:022708, Feb 2012.

- [38] K.-J. Yuan, X.-B. Bian, and A.D. Bandrauk. Two-center interference in molecular photoelectron energy spectra with intense attosecond circularly polarized xuv laser pulses. *Phys. Rev. A*, 90:023407, Aug 2014.
- [39] L. Chen, C. Huang, X. Zhu, P. Lan, and P. Lu. Molecular photoelectron holography by an attosecond xuv pulse in a strong infrared laser field. *Opt. Express*, 22(17):20421–20431, Aug 2014.
- [40] M. Nisoli, P. Decleva, F. Calegari, A. Palacios, and F. Martín. Attosecond electron dynamics in molecules. *Chem. Rev.*, 16, 2017.
- [41] A. Palacios, A. González-Castrillo, and F. Martín. Molecular interferometer to decode attosecond electronuclear dynamics. *PNAS*, 111, 2014.
- [42] D. Jelovina, J. Feist, F. Martín, and A. Palacios. A pump-probe scheme with a single chirped pulse to image electron and nuclear dynamics in molecules. *New Journal of Physics*, 20, 2018.
- [43] M. Lewenstein, Ph. Balcou, M. Yu. Ivanov, Anne L’Huillier, and P. B. Corkum. Theory of high-harmonic generation by low-frequency laser fields. *Phys. Rev. A*, 49:2117–2132, Mar 1994.
- [44] C.D.T. Runge. Über die numerische auflösung von differentialgleichungen. *Mathematische Annalen*, 46:162–178, 1895.
- [45] W. Kutta. Beitrag zur näherungsweise integration totaler differentialgleichungen. *Z Math Phys*, 46:435–453, 1901.
- [46] S. Borbély, G.Zs. Kiss, and L. Nagy. The excitation and ionization of the hydrogen atom in strong laser fields. *Central European Journal of Physics*, 8:249, 2010.
- [47] G.Zs. Kiss, S. Borbély, and L. Nagy. Momentum space iterative solution of the time-dependent schrödinger equation. *AIP. Conf. Proc.*, 1564:78, Nov 2013.
- [48] V. Hernández, J.E. Roman, and V. Vidal. SlepC: A scalable and flexible toolkit for the solution of eigenvalue problems. *ACM Trans. Math. Software*, 31(3):351–362, 2005.
- [49] C. Lanczos. *Journal of Research of the National Bureau of Standards*, 45(4):255–282, 1950.
- [50] A.N. Krylov. Translated from russian into english: On the numerical solution of equation by which are determined in technical problems the frequencies of small vibrations of material systems. *Izvestija AN SSSR (News of Academy of Sciences of the USSR)*, 7:491–539, 1931.
- [51] A. Tóth, S. Borbély, G.Zs. Kiss, G. J. Halász, and Á. Vibók. Towards the full quantum dynamical description of photoninduced processes in D_2^+ . *J. Phys. Chem. A*, 120:9411, 2016.
- [52] C. Amovilli and N.H. March. Characterization of potential energy curves for H_2^+ and H_2 by local values of electron density. *Chemical Physics*, 146:207–210, Sep 1990.
- [53] G.Zs. Kiss, S. Borbély, and L. Nagy. Efficient numerical method for investigating diatomic molecules with single active electron subjected to intense and ultrashort laser fields. *AIP Conf. Proc.*, 1916:20010, 2017.
- [54] K.-J. Yuan, H. Lu, and A.D. Bandrauk. Linear- and circular-polarization photoionization angular distributions in H_2 and H_2^+ by attosecond xuv laser pulses. *Phys. Rev. A*, 83:043418, Apr 2011.
- [55] L. Czipa and L. Nagy. Two-center interference in the ionization of H_2 by ion impact: Comparison of different models. *Phys. Rev. A*, 95:062709, Jun 2017.
- [56] L. Nagy, S. Borbély, and K. Póra. Interference effects in the photoionization of molecular hydrogen. *Phys. Lett. A*, 327:481–489, 2004.